SOFIA UNIVERSITY "ST. KL. OHRIDSKI", FACULTY OF PHYSICS
DEPARTMENT OF CONDENSED MATTER PHYSICS
AND MICROELECTRONICS

Assoc. prof. Vesselin Todorov Donchev

"Surface photovoltage spectroscopy of semiconductor optoelectronic materials and nanostructures"

SYNOPSIS

of the thesis to obtain a scientific degree
"Doctor of Science"

Professional field 4.1 "Physical Sciences"

Sofia, 2022

The thesis was discussed and scheduled for defence by the Department Council of the Department of Condensed Matter Physics and Microelectronics, Faculty of Physics at Sofia University "St. Kliment Ohridski", which took place on 06.07.2022.

CONTENTS

Introduction

The progress in semiconductor optoelectronic materials is one of the main factors for the fast development of semiconductor optoelectronics. The development of nanotechnology together with the deeper understanding of the underlying physics and new device concepts have led to a variety of semiconductor quantum heterostructures that are more and more used in the fabrication of light emitters and detectors resulting in devices with improved parameters and qualitatively new functionalities [1]. Despite numerous advances, research into such nanostructures continues looking for new material combinations and more complex integrated systems with reduced size and energy consumption and increased functionality and energy efficiency. At the same time, these complicated nanostructures allow the investigation of various phenomena interesting for the fundamental nano-physics.

Photovoltaics (PV) is a key optoelectronic technology to deliver electricity in sufficient quantities, at an affordable cost, and in a sustainable manner. Although reliable Si-based PV systems are commercially available and widely applied, novel PV materials and architectures are under extensive quest and development to pave the way for the next generation PV, which should overpass the Shockley-Queisser efficiency limit (~33 %) and become a major source of sustainable energy. Combining two or more p-n junctions with complementary absorption spectra leads to the so-called multijunction solar cells which are expected to outperform single-junction devices. The bandgap combination of the sub-cells and the crystal quality are key factors for further improvements in the overall cell efficiency. In this connection, there has been great interest in dilute nitride III-V-N materials during the last two decades. Their advantage over other materials is the possibility to adjust the bandgap around 1 eV while maintaining nearly lattice-matching to a GaAs substrate. Nevertheless, there are still unresolved problems related to trap-assisted recombination and low minority carrier diffusion lengths.

The successful design and fabrication of complex optoelectronic materials and nanostructures with required properties and quality need the feedback obtained by various relevant characterization techniques. Surface photovoltage spectroscopy (SPS), which is based on analysing illumination-

induced changes in the surface potential that are called surface photovoltage (SPV) has a special place as it offers many advantages over other characterisation techniques [2]. As the SPV arises from the spatial separation of the photogenerated electrons and holes the analysis of the results provides information on both light absorption properties and transport properties of charge carriers in the semiconductor sample. Thus, SPS gives more information as compared to optical absorption spectroscopy and contrary to the latter can be applied to structures grown on non-transparent substrates, which is often the case with nanostructures. Compared to photoluminescence (PL) which reveals the radiative optical transitions with the lowest energies, SPS provides information on the electronic transitions between both ground and excited states. The method is contactless and non-destructive and can be performed *in-situ* and *ex-situ*. It is characterized by a high sensitivity [2,3], which allows obtaining information on the surface, interface and bulk properties even at room-temperature operation. The study of SPV begins in the early 1950s. Over the years SPS has continuously evolved in terms of experimental tools and methods and algorithms for data analysis. Nevertheless, there are still open questions concerning the in-depth and correct data interpretation and the application to complex nanostructures.

The work presented in the thesis addresses some open questions related to the SPS and applies this method to study semiconductor nanostructures and bulk materials prospective for optoelectronic and photovoltaic applications. The purposes of the work can be grouped in three directions:

- design, construction and improvement of the SPS setup and measurement procedure,
- developing novel approaches for retrieving information from the SPV spectra, and
- the application of the developed setup and methodology in the study of various materials.

The thesis includes an introduction, 4 chapters, 85 figures, 5 tables, main results and contributions, a list of publications included in the thesis, and a list of references.

Chapter 1 gives a background on the semiconductor nanostructures, GaAs-based dilute nitride materials and the SPS method. Chapter 2 describes the experimental details for SPS in the chopped light geometry known also as metal-insulator-semiconductor (MIS) operation mode [2]. The measurement procedures and the developed methodology for retrieving information from the SPV spectra are presented. Special attention is paid to the useful information that can be derived from the analysis of the SPV phase spectrum, emphasizing the need for parallel analysis of the SPV amplitude and SPV phase. Chapter 3 presents the SPS investigations of four types of semiconductor nanostructures designed for optoelectronic applications - i) AlAs/GaAs superlattices with GaAs embedded quantum wells; ii) interdiffused InAs/InGaAlAs quantum dashes-in-quantum well structures for light emitters; iii) InAs quantum dot-in-quantum well structures for infra-red photodetectors, and iv) multi-layer structures with InP/GaAs type-II quantum dots. Chapter 4 is devoted to the SPS studies of photovoltaic materials, namely Si nanowires and GaAs-based diluted nitrides layers and solar cell structures.

CHAPTER 1. BACKGROUND

Chapter 1.1 provides basic information on semiconductor nanostructures emphasizing their unique properties leading to various applications in optoelectronic and electronic devices with improved parameters and qualitatively new functionalities. It includes also a brief overview of SPS investigations of nanostructures in a historical plan.

Chapter 1.2 reviews the GaAs-based dilute nitrides materials that are discussed in the thesis, namely GaAsN, InGaAs(Sb)N and GaAsSbN. Their main properties and applications in multijunction solar cells are presented. The issues related to the epitaxial growth of bulk layers, in particular employing liquid phase epitaxy (LPE) are pointed out. It is emphasized that SPS has been rarely used in the study of such materials, as well as that few reports exist on LPE-grown dilute nitrides.

Chapter 1.3 describes the basic principles of SPV generation, emphasizing the two steps of this process, namely i) optical generation of free carriers and ii) their separation in space. The SPS technique is applicable also to

study carrier generation and redistribution processes in the vicinity of buried interfaces because the illumination-induced changes of the interface potential propagate to the sample surface where they are detected as SPV signals. The main experimental methods used for SPV measurement are briefly reviewed – the *Kelvin probe technique* and the *metal-insulator-semiconductor operation mode*. This chapter ends with a description of the SPS application for assessing the minority carrier diffusion length in semiconductor materials.

CHAPTER 2. EXPERIMENTAL DETAILS AND METHODS

2.1. Experimental setup and measurement procedures for SPS in MIS operation mode

The experimental setup for surface photovoltage spectroscopy in MIS operation mode has been developed and improved over the years under the supervision of the author of several bachelor students and PhD students.

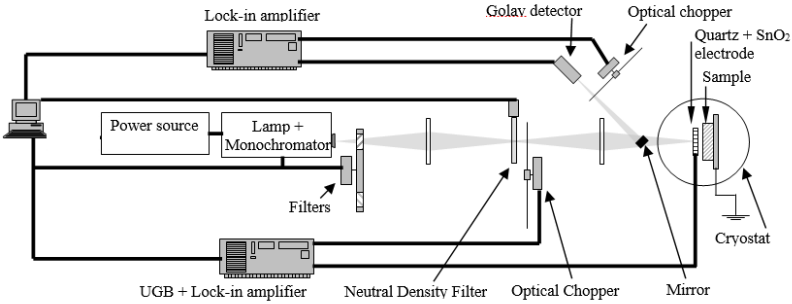

Figure 2.1. *Schema of the* ***e****xperimental setup for SPS.*

Figure 2.1 presents a schema of the experimental setup. The sample surface is illuminated through a semi-transparent electrode using a 250W halogen tungsten lamp along with a 0.22m SPEX grating monochromator, filters to cut off the high-order diffraction and an optical chopper (PTI OC4000 or 300CD). An SR830 Lock-in amplifier is used to measure the amplitude and phase of the SPV signal. The scanning is from long toward short wavelengths keeping the photon flux density Φ constant at each wavelength. For that purpose, part of the light is deflected with a small mirror towards ан Oriel IR50 Golay detector (which has a flat spectrum) through a second optical chopper (8 Hz) and the signal from the detector is fed to a lock-in amplifier (Brookdeal 9530). This feedback is used to adjust the position of a neutral density filter with graded optical density, thus achieving a quasi-real-time control of the photon flux density for each wavelength with an accuracy of about 1 %. For the spectral

range 800 - 1800 nm we use a grating with 600 gr/mm blazed at 1000 nm (dispersion 8 nm/mm), while for the 450 – 900 nm range the grating is with 1200 gr/mm blazed at 500 nm (dispersion 4 nm/mm). The monochromator is equipped with a series of slits from 0.25 mm to 5 mm that are used to achieve a given spectral resolution and adjust the excitation level in a certain range.

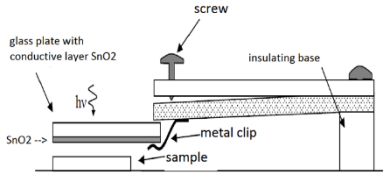

***Figure 2.2**. Schema of the sample and the probe holder used in the cryostat.*

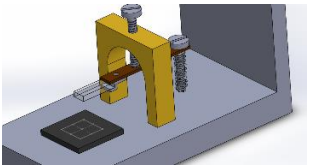

***Figure 2.3**. Schema of the sample and probe holder used outside the cryostat.*

The sample is mounted on a grounded copper platform. The semi-transparent electrode (further called probe) is a SnO_2 film deposited on the bottom side of quartz glass. Its transmission is constant in the working wavelength range with no interference effects. There are two arrangements for fixing and adjusting the probe. The first one (Fig. 2.2.) is for use in the continuous flow Leybold-Heraeus optical cryostat (65 – 300K), while the other (Fig. 2.3.) – is used in ambient conditions. In both cases, the arm, which holds the probe can be bent downward to gently press it to the sample. A sheet of mica (typically 15-25 μm) is placed in some cases between the sample and the probe. The second arrangement assures a better control of the height and angle of the probe relative to the sample and allows easier and faster change of samples up to 10×20 mm^2.

Figure 2.4 (a) shows the equivalent circuit of the measurement scheme, which acts as a voltage divider. Neglecting C_{par} it is easy to show that the voltage transmission coefficient, defined as the ratio between the measured δV_{meas} and true SPV value δV_s is given by the expression (2.1):

$$k = \frac{\delta V_{meas}}{\delta V_s} = \frac{1}{\left(1 + \frac{R_s}{R_i} + \frac{C_i}{C_{ins}}\right) + j\left(\omega C_i R_s - \frac{1}{\omega C_{ins} R_i}\right)} \qquad (2.1.)$$

It is seen that δV_{meas} is closer to δV_s if the following relations hold: $R_i >> R_s$; $C_{ins} >> C_i$; $(R_i C_{ins})^{-1} << \omega << (R_s C_i)^{-1}$. The first two relations define the amplitude of *k*. The last one defines the frequency domain in which the complex part of (2.1.) does not affect the amplitude or the phase of the measured signal.

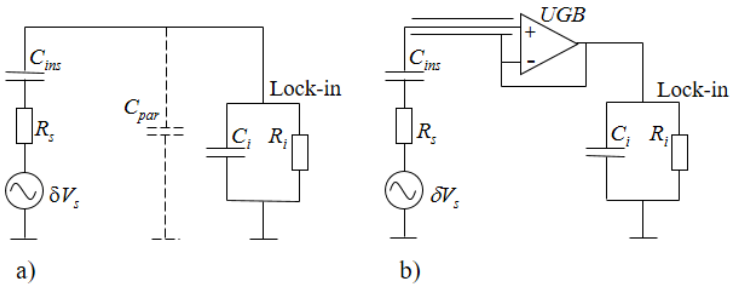

Figure 2.4. *Equivalent circuit of the measurement scheme in the MIS operation method: a) without voltage repeater; b) with voltage repeater. The sample is represented as an ac voltage source with resistance R_s. C_{ins} – capacitance of the MIS structure, C_{par} – parasitic capacitance of the cables, C_i – input capacitance of the lock-in, R_i – input resistance of the lock-in* [4].

The parasitic capacitance C_{par} is added to C_i and thus has a negative effect on both amplitude and frequency characteristics of *k*. To address this problem, the SPV signal from the probe electrode relative to the ground is fed to a voltage repeater consisting of a high-impedance unity gain buffer (UGB) with operational amplifier LF356. In addition, the shield and the core of the cable carrying the SPV signal are kept at the same potential to reduce the cable capacitance effect. For that purpose, the cable shield is electrically connected to the UGB output (see Fig.2.4 (b)).

The voltage transmission coefficient $|k|$ of the electric circuit is measured in the following way. The sample back contact is disconnected from the ground and a known external ac voltage is applied between this contact and the ground, keeping the MIS capacitor in dark. Then $|k|$ is equal to the ratio between the voltage measured by the circuit and the known external voltage. Typical values are between 0.3 and 0.4 when a mica sheet is placed between the sample and the probe.

To study the SPV phase delay relative to the light excitation in a correct way it is necessary to consider or eliminate the possible phase shifts between i) the SPV and the voltage measured by the Lock-in amplifier and ii) the light modulation and the reference signal generated by the optical chopper. The first issue is solved during the determination of the voltage transmission coefficient by recording the phase delay of the measured voltage relative to that of the known external voltage. For the frequencies used in the SPV measurements reported in the thesis, this delay has been negligible in most of the cases. To address the second issue a fast photodetector is positioned in the place of the sample and the measured phase delay is recorded. It is eliminated by the phase shifter of the PTI OC4000 chopper or by setting this phase value of the SR830 Lock-in. The procedures to eliminate undesired phase shifts enable defining the zero value of the SPV phase - it is the phase of the light excitation. Thus, any nonzero phase values observed in the experiment are attributed to processes taking place in the sample, which allows for investigating their origin and kinetics.

The SPV measurements presented in the thesis have been performed at room temperature (unless otherwise stated) with normal incident light with constant photon flux density (between 1×10^{13} and $5\times10^{14}\text{cm}^{-2}\text{s}^{-1}$ depending on the concrete case) scanning from large towards low wavelengths.

2.2. The advantages of using the SPV phase spectra

2.2.1. Original approaches concerning the SPV phase

It is widely accepted that the SPV amplitude emulates the spectrum of the optical absorption coefficient, $\alpha(h\nu)$. On the contrary, the SPV phase was the subject of relatively fewer reports [5–7]. SPV phase spectra were seldom

reported and discussed mainly in terms of relative changes of the phase at certain critical wavelengths without defining the zero-phase value [5,7].

First original approach. The phase φ of the SPV signal, corresponding to a single SPV generation process, is related to the direction of the energy band bending at the place where the signal is generated.

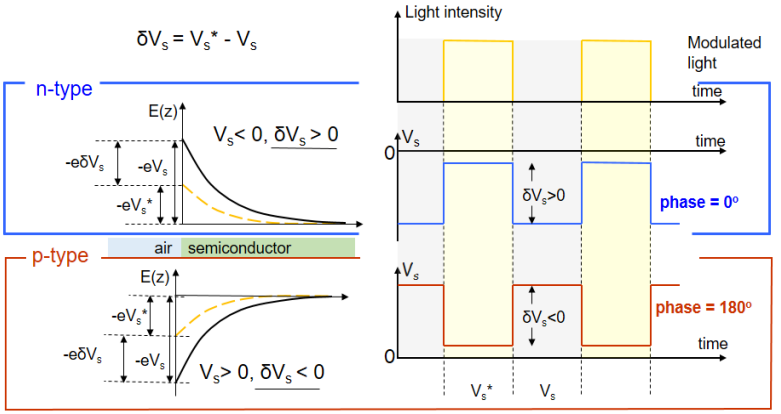

Figure 2.5. *Left: Surface band bending in dark (solid lines) and under illumination (dashed lines) of the CB edge in n-type and p-type semiconductors under depletion; Right: Surface potential as a function of time in the case of n-type and p-type semiconductors compared to the light excitation pulses in the ideal case where no phase delay exists* [4].

This is illustrated in Fig. 2.5. for the case where the energy band bending decreases under illumination, which is the most common case. For upward band bending the surface potential $V_s < 0$, therefore its change under light $\delta V_s > 0$, while for downward band bending the opposite is true: $V_s > 0$, $\delta V_s < 0$. In the ideal case of very fast carrier generation, redistribution and recombination processes, which do not introduce any phase delay of the SPV signal, the SPV phase, measured relative to the light excitation, would be zero for upward ($\delta V_s > 0$) and 180° for downward band bending ($\delta V_s < 0$).

In the real case, due to the retardation of the signal relative to the light excitation, the SPV phase is in the IVth quadrant for upward and in the IInd quadrant for downward band bending. The SPV phase delay $\Delta\varphi$ is therefore calculated as $\Delta\varphi = |\varphi|$ for upward, and $\Delta\varphi = 180^o - \varphi$ for downward band bending, where φ is the measured phase value. In other words, the phase is in the IVth quadrant (IInd quadrant) when the photogenerated electrons move towards the bulk (surface) and holes move towards the surface (bulk). It is recommended to consider the SPV phase spectrum rather than the value of φ at a single photon energy $h\nu$. When scanning from low to high $h\nu$ the onset of the band-to-band optical transitions usually gives rise to a relatively fast SPV formation process with strong amplitude. As a result, φ changes towards $\pm 0^o$ in the case of upward and towards $\pm 180^o$ in the case of downward band bending. In both cases the phase delay $\Delta\varphi$ decreases.

The fact depicted above can be used to determine the type of the investigated semiconductor. Indeed, most semiconductor surfaces are either depleted or inverted at equilibrium, which means that the surface band bending is upward (downward) for an *n*-type (*p*-type) semiconductor. Therefore, a bandgap-related step in the phase spectrum approaching the phase toward $\pm 0^o$ ($\pm 180^o$) will indicate an n-type (p-type) semiconductor. A limitation of this approach arises in the case of small surface band bending, where the Dember effect dominates over the band-bending-related contribution to the measured SPV signal. In this case, if the electrons diffuse faster (slower) than the holes, the SPV phase is in the IVth (IInd) quadrant. Another point to have in mind is that in accumulated surfaces the band bending is opposite to the one discussed above and the quadrants of the SPV phase will be swapped.

Second original approach. It concerns the relation between the SPV phase and the free carrier generation rate $\beta\alpha(h\nu)\Phi$ (β is the quantum efficiency). To the best of our knowledge, there are neither reports on numerical studies nor analytical expressions derived for these dependencies, yet. Below we discuss qualitatively how the increased free carrier generation rate leads to a decrease in the SPV phase delay.

Following the discussion in [6], the equivalent circuit of the semiconductor under chopped light excitation is presented in Fig. 2.6. It includes a photocurrent

source i_{ac}, the capacitance C_{SCR} of the surface space charge region (SCR) and a conductance G that represents the various loss mechanisms due to carrier recombination [6]. Considering that $\delta V_s = i_{ac}Z$ the impedance Z of the circuit induces an SPV phase delay $\Delta\varphi$ given by the following relation

$$tg(\Delta\varphi) = \omega \frac{C_{SCR}}{G} \ . \tag{2.2}$$

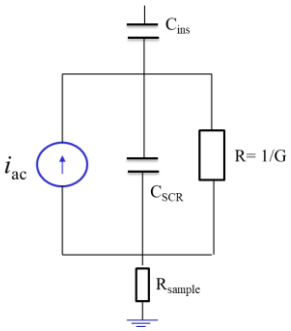

Figure 2.6. *Equivalent schema of the semiconductor under chopped light excitation acting as the ac voltage source δV_s from Fig. 2.4. The capacitance of the MIS structure C_{ins} and the sample resistance R_{sample} are also shown.*

Extending the discussion from [6] to consider the SPV phase dependence on $\beta\alpha(h\nu)\Phi$ we can say that according to Eq. (2.2), $\Delta\varphi$ decreases when G increases and increases when C_{SCR} increases. With increasing the free carrier generation rate, the SCR width w usually decreases due to the screening of the surface electric field by photocarriers, thus leading to an increase in the capacitance C_{SCR}. This would increase $\Delta\varphi$. However, considering that $w \sim \sqrt{V_s}$, this effect should be very weak at sufficiently large surface band bending and low and moderate excitation levels, because in such cases the change of the surface potential δV_s is much less than its dark value V_s.

The conductance G is inversely proportional to the effective carrier lifetime [6] and therefore will increase when it decreases. The increase of the free carrier generation rate can lead to a decrease in the effective carrier lifetime via different mechanisms depending on the peculiarities of the semiconductor sample and the experimental conditions. Such mechanisms lead to a non-linear recombination regime.

1) *Trap-assisted recombination.* Many semiconductors contain carrier traps in the bandgap, which are effective recombination centres. Under bipolar excitation ($\Delta n = \Delta p$) with low and moderate levels, these recombination channels may not be saturated and trap-assisted recombination of free electrons and holes may dominate or have an essential contribution. As discussed in [8] in this case the recombination kinetics is non-linear since the concentration of excess minority carriers cannot be neglected relative to their equilibrium concentration, which is very low. This results in an excitation-dependent carrier lifetime even at low and moderate excess carrier generation rates.

2) *Shallow traps*. In some materials e.g. CdS impurities states with shallow levels in the bandgap can trap electrons or holes for a while and then thermally release them at some later time [9]. As a result, the effective carrier lifetime is larger than its "normal" value without traps. This effect is observable at low excitation levels. With increasing the carrier generation rate these traps are gradually saturated and their effect becomes more and more negligible. This results in a decrease in the effective carrier lifetime.

3) *Surface states.* During the scan from low toward high $h\nu$ with constant photon flux, approaching and passing through the bandgap energy the optical absorption increases dramatically. As a result, the region where the photocarriers are generated shrinks progressively toward the surface of the semiconductor sample. This increases the role of the recombination via surface states and consequently decreases the effective carrier lifetime τ_{eff} given by

$$1/\tau_{\text{eff}} = 1/\tau_{\text{bulk}} + 1/\tau_{\text{surf}}. \qquad (2.3)$$

The mechanisms of non-linear recombination described above explain how the increased free carrier generation rate decreases the effective carrier lifetime and therefore increases G in Eq. (2.2). This effect is expected to be stronger than the effect of capacitance C_{SCR} reduction in most cases used in the current study. Therefore, increasing the free carrier generation rate leads to a decrease in the SPV phase delay relative to the light modulation, i.e. to an anticlockwise change of the SPV phase. The relative contribution of each of these mechanisms depends on the sample characteristics and experimental conditions.

The dependence of $\Delta\varphi$ on $\beta\alpha(h\nu)\Phi$ is non-linear and complicated. However, as δV_s is a monotonous function of the excess carrier concentration Δn, one expects that, similarly to the phase delay of $\Delta n(t)$ (see [10]), $\Delta\varphi$ asymptotically approaches toward 0^o (90^o) for high (low) values of $\alpha(h\nu)\Phi$ and low (high) values of the light modulation frequency f. Therefore, $\Delta\varphi$ will be more sensitive to changes of $\beta\alpha(h\nu)\Phi$ and f when their values are far from the extreme cases of very high or very low values. Consequently, at intermediate values of $\beta\alpha\Phi$ and f the SPV phase spectrum will better reveal small features in the $\alpha(h\nu)$ spectrum. It is important to note that these experimental conditions are usually used in SPV experiments.

The mechanisms described above can explain the strong decrease of the SPV phase delay in the spectral region corresponding to the onset of the band-to-band optical transitions, as well as the peak features in the SPV phase spectrum of QWs arising at the energies of the excitonic transitions (see Sec.3.1.).

The qualitative discussion presented above needs to be complemented by numerical simulations of the SPV generation processes to understand in-depth the SPV phase delay relative to the light modulation and describe quantitatively its dependence on the optical absorption coefficient and the photon flux density. Such simulations will be the subject of future studies.

2.2.2. Vector model for representing the SPV signal

The analysis from the previous section implies that it is important to examine simultaneously both SPV amplitude and SPV phase spectra to achieve a correct understanding of the experimental data. To facilitate such analysis a vector model for the SPV signal is developed [11] representing the SPV signal by a radial vector with the same magnitude as the SPV amplitude and angle relative to the X-axis equal to the SPV phase. The change in the SPV amplitude leads to a change in the vector's magnitude, while the SPV phase change is represented by vector rotation. According to the adopted definition of the SPV phase, in the case of very fast processes the SPV vector angle will be close to 0° (180°) for upward (downward) energy band bending. In the real case, the SPV vector, corresponding to a single SPV generation process is in the IVth (IInd) quadrant if the position where it arises has an upward (downward) energy band

bending relative to the bulk. In the case of non-linear recombination increasing the free carrier generation rate will not only increase the magnitude of the SPV vector but will also rotate it anticlockwise. In the case of Dember effect domination, the angle of the SPV vector depends on the type of carriers that are more mobile.

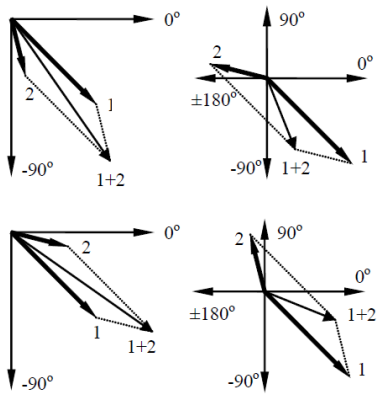

Figure 2.7. *Different combinations of the magnitudes and angles of the two SPV vectors ("1" and "2"), leading to a change in magnitude and orientation of the resulting overall SPV vector ("1+2") relative to vector 1.*

The vector model is especially useful when more than one SPV generation processes occur in the same spectral range. A typical example is found in multi-layered samples, where the absorption of the substrate and the layers (with different bandgaps) often results in SPV processes with different amplitudes and phases. Such a situation can be modelled by the addition of a second SPV vector corresponding to the new SPV generation process when reaching a certain wavelength range to the SPV vector describing the SPV process already existing at the previous wavelengths. The resulting overall vector will be rotated towards the second vector. Thus, both SPV amplitude and phase can change in both directions and one of the four possible combinations shown in Fig. 2.7 will take place depending on the concrete amplitudes and phases of the two processes [11].

It is worth noting that the measured SPV signal corresponds to the vector sum of all active processes and deriving information about the individual processes requires further effort. A quantitative analysis of the SPV vector addition requires assuming that the two processes are independent. In many cases, this is not strictly accomplished and therefore it is better to only focus on the qualitative analysis.

2.3. Conclusions

An experimental setup and measurement procedure for SPS in the MIS operation mode are developed. For the first time, the zero value of the SPV phase has been defined and used for the interpretation of the SPV amplitude and phase spectra. The SPV phase is in the IV^{th} (II^{nd}) quadrant for upward (downward) energy band bending. The decrease of the SPV phase delay with increasing the free carrier generation rate has been qualitatively explained by proposing several mechanisms that decrease the excess carrier lifetime and lead to non-linear recombination. In such cases, the SPV phase spectrum reflects the features of the optical absorption coefficient spectrum. The developed vector model of the SPV signal facilitates the combined analys of the SPV amplitude and phase spectra leading to a deeper understanding of the experimental data. It is especially useful when more than one SPV generation processes occur in a given spectral range.

CHAPTER 3. SPS of NANOSTRUCTURES for OPTOELECTRONIC APPLICATIONS

3.1. AlAs/GaAs superlattices with GaAs embedded quantum wells

The superlattices (SLs) with embedded quantum wells (EQWs) represent SLs in which one or more of the QWs are wider or narrower than the others. Short-period AlAs/GaAs SLs containing GaAs EQWs have received considerable interest because they present new physical properties often different from those of single QWs and unperturbed SLs and on the other hand have many advantages in comparison with single GaAs QWs with homogeneous AlGaAs alloy barriers. This section presents our original SPS studies of short-period AlAs/GaAs SLs with GaAs EQWs reported in papers **F2, F4 – F6** and **O1**. At the time they were performed, SPS studies of only single GaAs/AlGaAs QWs and SLs were reported in the literature [12,13].

Two types of samples prepared by MBE in EPFL, Switzerland are studied. Their structure is schematically represented in Fig. 3.1.1.

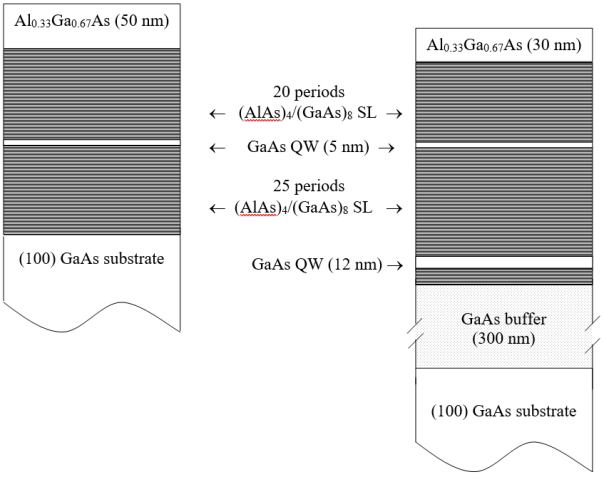

***Figure 3.1.1**. Schematic representation of the experimental samples types A (left) and type B (right)*

3.1.1. AlAs/GaAs superlattices with two GaAs embedded quantum wells (samples type B)

The samples were grown at 580°C on n-type (100) GaAs substrates (10^{18} cm^{-3}). The buffer layer and the rest of the structure are nominally undoped but one expects slight p-type doping due to carbon incorporation.

Figure 3.1.2. presents typical SPV amplitude and phase spectra of a sample type B recorded with photon flux density $\Phi \approx 4\times10^{13} cm^{-2}s^{-1}$. Steps A (1.421 eV) and H (1.815 eV) correspond to the onset of the band-to-band absorption in the bulk GaAs (buffer layer and substrate) and in the AlGaAs cap layer, respectively.

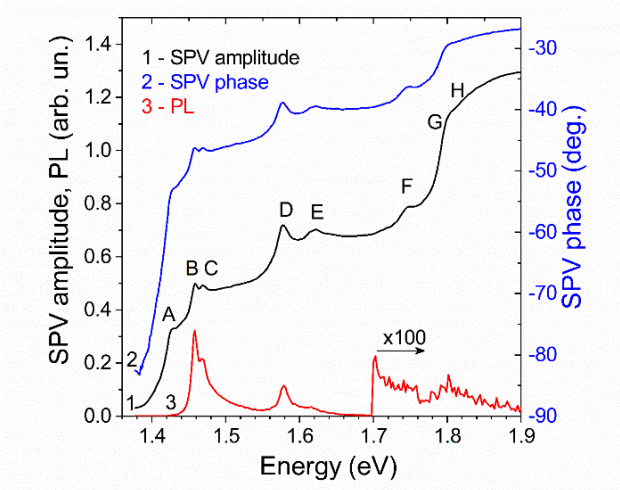

Figure 3.1.2. *Room temperature SPV amplitude (curve 1), SPV phase (curve 2) and PL (curve 3) spectra of an $(AlAs)_4/(GaAs)_8$ SL with two GaAs EQWs grown on a 300 nm GaAs buffer layer. The PL spectrum for energies higher than 1.7 eV is multiplied by a factor of 100* [14].

To interpret the spectral features B–G, we have compared their energy positions (given in the 3rd column of Table 3.1.1) with the optical transition energies calculated in frames of the envelope function approximation (EFA). In

the calculations of the EQW bound states, we consider a model structure with a semi-infinite $Al_{0.33}Ga_{0.67}As$ cap layer and GaAs substrate. The interface grading is also taken into account following our model considering a diffuse profile of the Al concentration [15]. In this model, the diffusion length L_D is a parameter determining the degree of interface grading. The non-abrupt concentration profile results in a graded potential profile in the growth direction, which affects the energies of the bound states. The one-band EFA equation is solved numerically by the finite differences method[1] for potential profiles corresponding to different L_D values. The 5th column of Table 3.1.1 presents the calculated optical transitions energies assuming an interface grading corresponding to a diffusion length of 3.7 monolayers (MLs) (=1.05 nm) in agreement with previous PL findings [15]. The last column gives the calculated transition energies, corrected for the exciton binding energies [16].

Table 3.1.1. Optical transitions and their energies (in eV) as determined by SPS, PL and EFA calculations assuming an interface grading, corresponding to a diffusion length of 3.7 ML (1.05 nm). The exciton binding energies are given in column 6 in meV. The last column represents the calculated values corrected for excitonic effects.

Transition	Label	SPS	PL	EFA calculations (L_D = 1.05 nm)		
					$E_{exciton}$	$E - E_{exciton}$
1	2	3	4	5	6	7
HH1-E1 (12 nm EQW)	B	1.458	1.458	1.462	9	1.453
LH1-E1 (12 nm EQW)	C	1.469	1.468	1.475	10	1.465
HH1-E1 (5 nm EQW)	D	1.579	1.579	1.594	12	1.582
LH1-E1 (5 nm EQW)	E	1.616	1.618	1.628	13	1.615
HH3 – E3(12 nm EQW)	F	1.741	….	1.748	9	1.739
HH3 (12 nm EQW) - E(SL)	F	1.741	….	1.757	9	1.748
HH(SL) - E(SL)	G	1.794	1.802	1.817	4	1.813

[1] The computer programme for EFA calculations was prepared by Nikolay Shtinkov.

The peaks B (1.458 eV) and C (1.469 eV) are identified as the heavy-hole (HH) and light-hole (LH) exciton peaks of the 12 nm EQW. The peaks D (1.579 eV) and E (1.616 eV) are identified as the HH and LH exciton peaks of the 5 nm EQW. The two steps, which start with the peak doublets B-C and D-E, correspond to the two-dimensional joint density of states in the 12 nm and 5 nm EQWs, respectively. Step F (1.741 eV) is ascribed to both the HH3-E3 transition in the 12 nm EQW and a mixed transition between the HH3 state of the 12 nm EQW and the SL electron miniband. Step G (1.794 eV) is due to the E-HH exciton and free carrier transitions in the SL.

The conclusions given above are supported by the PL spectrum in Fig. 3.1.2. Within the experimental error (~4 meV) the SPV peaks from B to E have the same energy positions as the four PL peaks originating from the HH and LH excitonic transitions in the two EQW. The comparison between the SPV and PL spectra also shows that the SPS is more informative than the PL.

The structures A-H observed in the amplitude spectrum (curve 1) in Fig. 3.1.2, are well resolved also in the SPV phase spectrum (curve 2), where they appear at the same energy positions. This supports the above-presented idea about the relation between the SPV phase and the optical absorption coefficient. The knee in the SPV phase spectrum, related to bulk GaAs band-to-band optical transitions (~1.421 eV) and the phase features corresponding to the EQW exciton absorption peaks correspond to phase changes towards -0^{o}, which shows that the energy bands in the structure are bent upward relative to the bulk. This is explained by the SCR existing at the interface between the epitaxial structure with slight residual p-type doping and the heavily n-type doped substrate. The SCR develops mainly in the structure and has an electric field directed towards the surface.

The photogenerated carriers in the EQWs escape towards the SL minibands via thermal emission and field-assisted tunnelling emission as in single QWs. The SCR electric field drives the excess electrons (holes) towards the bulk (surface) which explains the phase values in the IV^{th} quadrant. A rough estimate of the built-in field shows that it is not enough to split the SL minibands into discrete levels. Consequently, the photocarrier transport in the SL occurs in the low electric field regime through resonant tunnelling in the SL minibands.

The excitation density dependence of the net contributions (after subtracting the background) of the SPV peaks B and D has been studied. A power-law dependence with a coefficient $\mu = 0.51$ up to the maximal photon flux density $\Phi_{max} = 5\times10^{14}$ cm^{-2}s^{-1} is found for the 12 nm EQW (peak B). For the 5 nm EQW (peak D) a satisfactorily fit is obtained in the range $\Phi \leq \sim 0.3\,\Phi_{max}$ (1.5×10^{14} cm^{-2}s^{-1}) with $\mu = 0.46$, while for larger Φ the dependence becomes weaker. These findings can be regarded as experimental confirmation of the theoretical predictions of Ruda and Shik for isolated QWs [17].

3.1.2. AlAs/GaAs superlattices with one GaAs embedded quantum well (samples type A).

The samples were grown by MBE at 600°C on two types of (100) GaAs substrates: semi-insulating (SI) and Si-doped (10^{18} cm^{-3}). No buffer layer was grown between the substrate and the first SL.

The SPV spectral features are identified based on comparison with PL results and EFA calculations of the optical transition energies. In the EFA calculations of the EQW bound states energies an interface grading corresponding to diffusion length L_D = 4.6 ML (1.30 nm) is assumed in agreement with previous PL studies [15]. The increased interface broadening as compared to the samples from the previous section can be accounted for by the absence of a buffer layer and the larger growth temperature.

3.1.2.1. Samples grown on n-GaAs substrates

Because the substrate is highly n-type doped and the epitaxial structure is nominally undoped, an SCR develops at the interface with upward energy band bending relative to bulk and a built-in electric field oriented towards the surface. It extends predominantly in the structure. Figure 3.1.3. displays typical SPV amplitude and phase spectra of these structures. The amplitude step in the range 1.40 – 1.55 eV originates from transitions in the GaAs substrate (E_g = 1.424 eV). Its n-type doping leads to an SPV vector in the IVth quadrant.

Above 1.550 eV the amplitude spectrum reveals two peaks ascribed to the E1-HH1 (1.597 eV) and E1-LH1 (1.639 eV) free exciton transitions in the EQW. Accordingly, the SPV phase also exhibits two dips at very close energies (E1-HH1 at 1.593 eV and E1-LH1 at 1.635 eV), corresponding to clockwise

rotation. The interaction between the SPV signals (vectors) from the substrate and the EQW is represented by the vector diagram in inset A of Fig. 3.1.3. The clockwise rotation of the overall SPV vector indicates that the EQW vector is closer to -90° than the vector of the substrate, which means that the SPV process from the EQW is slower. For higher $h\nu$ after the peaks, the SPV amplitude has a constant value, which reveals the 2D joint density of states in the EQW.

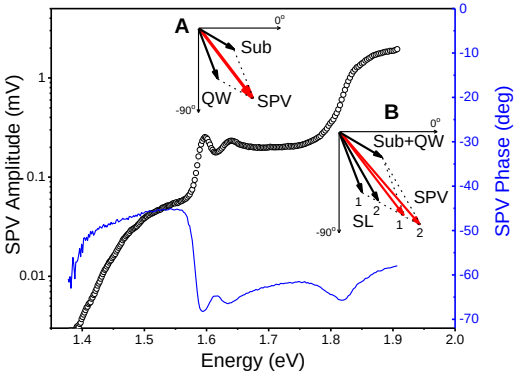

Figure 3.1.3. *SPV amplitude (open circles) and phase (solid line) spectra of a sample grown on n-type GaAs substrate. Insets A and B are vector diagrams showing the interaction of different SPV processes for two different spectral regions. The overall SPV vector is given in red. Sub, QW and SL denote the substrate, EQW and SL vectors.*

Above 1.75 eV the SPV amplitude spectrum reveals a step with an inflection point at 1.822 eV associated with transitions between the electron and hole mini-bands of the SL. The phase of the overall SPV signal is again in the IVth quadrant in agreement with the upward energy band bending. However, it shows a non-monotonous behaviour with the photon energy, which is explained as follows. The initial rise in the SL absorption and correspondingly of the SL vector's magnitude leads to clockwise rotation of the overall SPV vector similar to the EQW absorption. However, after 1.820 eV, the SL vector starts to rotate counter-clockwise and this leads to counter-clockwise rotation of the overall

vector. This behaviour is illustrated in inset B of Fig. 3.1.3, where the overall SPV vector is represented in red for two subsequent SL vectors, following the above scenario. Near the end of the step (1.850 eV), the SL signal is one order of magnitude larger than the signals from the substrate and the EQW and it dominates the spectrum. The counter-clockwise rotation of the SL vector occurring with the increase of the optical absorption suggests the appearance of a non-linear recombination regime.

Table 3.1.2. Experimental and calculated optical transition energies for the samples with one EQW. The values obtained from SPS for the samples grown on n-GaAs and SI GaAs are given.

Transition	SPS	PL	EFA calculations (L_D = 1.3 nm)		
	E (eV)	E (eV)	E (eV)	E_{exc} (meV)	$E - E_{exc}$ (eV)
E1-HH1	1.597, 1.603	1.599	1.605	12	1.593
E1-LH1	1.639, 1.643	1.625	1.636	13	1.623
E-HH (SL)	1.822	1.838	1.828	4	1.824

The experimental and calculated optical transition energies for the EQW and the SL are given in Table 3.1.2. The calculated energies corrected for excitonic effects are given in the last column. They show good agreement with the experimentally obtained values.

3.1.2.2. Samples grown on SI GaAs substrates

Figure 3.1.4. shows typical SPV amplitude and phase spectra of a sample grown on SI GaAs substrate. The spectral range of the EQW and SL reveals a behaviour opposite to that in Fig. 3.1.3. This is due to the different substrate types, as explained below.

Because in SI GaAs the energy bands are virtually flat, Dember effect is the dominant cause for the generation of photovoltage. Since in GaAs the electrons diffuse faster than holes, it gives SPV phase in the IVth quadrant. The large substrate signal dominates the SPV in the whole spectral range. The quantum structure is nominally undoped, but as the most common residual

impurity introduced during the MBE growth is carbon, one can expect slight p-type doping. As a result, the energy bands in the epitaxial structure are bent downward in the direction toward the surface. Therefore, the SPV processes generated from the EQW and SL can be manifested by vectors in the IInd quadrant. These vectors form an obtuse angle with the substrate vector (see the vector diagram in Fig. 3.1.4) and the growth of their magnitude results in a decrease in the magnitude and counter-clockwise rotation of the overall SPV vector. This is the case for both, the EQW and the SL spectral ranges - where the SPV amplitude decreases and the SPV phase increases. Due to the large substrate signal, the contributions of the E1-HH1 and E1-LH1exciton transitions in the EQW are seen as small dips in the amplitude spectrum at 1.603 eV and 1.643 eV, respectively. Accordingly, the phase reveals small peaks at the same energies. The contribution of the SL is well resolved due to its larger volume as a negative step in the amplitude and a positive step in the phase, in agreement with the vector diagram in the inset.

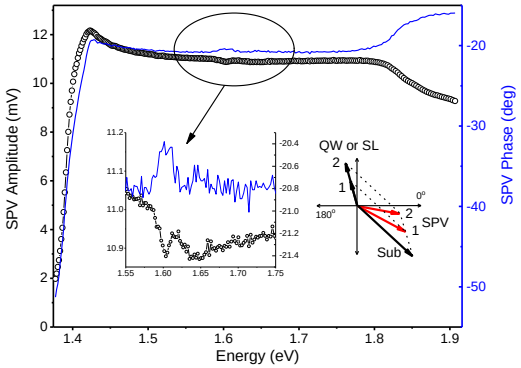

Figure 3.1.4. *SPV amplitude (open circles) and phase (solid line) spectra of a sample grown on SI GaAs substrate. Insets: magnified amplitude and phase spectra in the EQW energy range; vector diagram showing the dependence of the overall vector (shown in red) on the growth of a vector in the IInd quadrant (EQW or SL absorption).*

3.1.3. Radiative recombination mechanisms in the GaAs quantum wells embedded in AlAs/GaAs superlattices

Typical PL spectra of samples A and B measured at different temperatures[2] are presented in Fig. 3.1.5. Peaks P1 and P2 are ascribed to optical transitions in the 12 nm EQW, while peaks P3 and P4 are attributed to the 5 nm EQW. The difference in P3 positions in samples A and B is due to different interface grading, as discussed above and in Ref. [18].

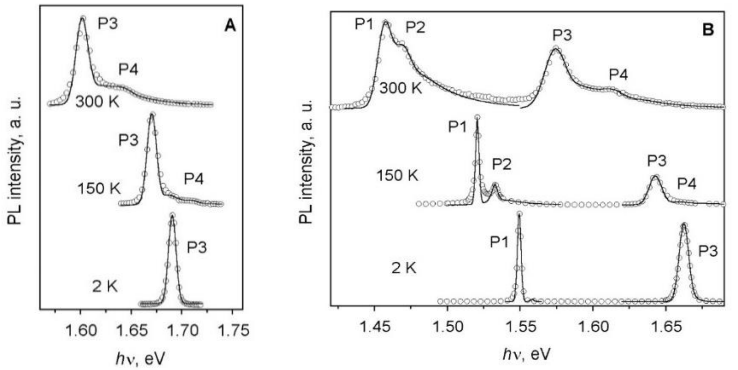

Figure 3.1.5*. PL spectra (circles) and fits of the PL peaks (lines) of samples A (left) and B (right).*

The PL line shapes are analysed by applying the model described in [19,20]. Two Gaussians, multiplied by the corresponding Boltzmann statistical distributions describe the discrete exciton lines (I_x) for the heavy-hole and light-hole exciton transitions. The free carrier recombination terms (I_c) include a broadened step-like two-dimensional density of states, multiplied by the free carrier Boltzmann statistical distribution and the two-dimensional Sommerfeld factor to take into account the Coulomb interaction between carriers. Thus, the emission intensity is a sum of the following terms where A_{xi}, E_{xi} and σ_{xi} (i = HH, LH) denote the amplitude, the energy and the broadening parameter of the

[2] PL spectra at low temperatures were recorded by Ivan G. Ivanov in Linkoeping University

exciton lines; A_{ci}, E_{ci}, σ_{ci} are the amplitude, the energy and the broadening parameter of the free-carrier recombination; and E_{bi} are the exciton binding energies:

$$I_{xi}(h\nu) = A_{xi} \exp\left[-\frac{(h\nu - E_{xi})^2}{2\sigma_{xi}^2}\right] \exp\left(-\frac{h\nu - E_{xi}}{kT}\right), \tag{3.1.1}$$

$$I_{ci}(h\nu) = A_{ci} \frac{1}{1+\exp\left(-\frac{h\nu - E_{ci}}{\sigma_{ci}}\right)} \exp\left(-\frac{h\nu - E_{ci}}{kT}\right) \times \frac{2}{1+\exp\left(-2\pi\sqrt{\frac{E_{bi}}{|h\nu - E_{ci}|}}\right)} \cdot \tag{3.1.2}$$

Table. 3.1.3. The ratio F/X of the contributions of free carriers (F) and free excitons (X) to the radiative recombination in samples type A and B for different temperatures.

T (K)	*F/X*		
	Type B		Type A
	12 nm EW	5 nm EW	5 nm EW
2	0	0	0
64	0.07	0.02	0.02
77	0.12	0.04	–
80	–	–	0.03
100	0.18	0.08	0.07
150	0.44	0.20	0.22
206	–	–	0.34
300	0.95	0.63	0.73

Figure 3.1.5. shows that the theoretical fits describe satisfactorily the main features of the experimental peaks. The contributions of free excitons (X) and free carriers (F) are obtained by integrating expressions (3.1.1.) and (3.1.2.), respectively over the photon energy. Table 3.1.3. represents the values of the ratio F/X at different temperatures in two samples (type A and B). At 2 K the radiative recombination 2 K is purely excitonic (F=0). With increasing the temperature, the free carrier contribution increases and so does the ratio F/X. Its

values are larger for the wider EQW in agreement with the smaller exciton binding energies in this case, which favours easier exciton ionization. At room temperature F is comparable to X, but free exciton recombination still prevails: F/X is in the range of 0.84 - 0.95 for the 12 nm EQW, and 0.63 - 0.82 for the 5 nm EQW in different samples. These findings show that free exciton recombination is dominant up to room temperature.

3.1.4. Conclusions

The exciton transition energies in the EQWs and the SLs determined by SPS are in very good agreement with the values found by PL and EFA calculations. The degree of interface grading has been assessed from the comparison between calculated and experimental transition energies. It is larger for samples grown at higher temperatures and without a buffer layer. The photocarriers escape from the EQW via thermal emission and field-assisted tunnelling and their transport in the SLs is in the low-electric-field regime through resonant tunnelling in the minibands. The SPV spectral shape in nanostructures can be significantly affected by the substrate type. Free excitons recombination dominates the PL emission up to room temperature.

3.2. Interdiffused InAs/InGaAlAs quantum dashes-in-quantum well structures for light emitters

Semiconductor quantum-dot heterostructures have been extensively studied because their low dimensionality is advantageous for the realization of high-performance optoelectronic devices. Various light emitters have been demonstrated based on InAs/GaAs quantum dots (QDs) with emission wavelengths from 1 to 1.3 μm. However, it is difficult to obtain emission wavelengths beyond 1.3 μm with this system. As an alternative, there has been an increasing interest in growing self-assembled InAs dots or dashes on InP substrates to reach the long-wavelength emission for optical fibre telecommunication, gas sensing, and molecular spectroscopy applications. However, the InAs/InP QDs and quantum dashes (QDH) emit around 1.6 μm and to achieve the wavelength of 1.55 μm, optimal for fibre telecommunication, further modification of their characteristics is necessary. This section describes our pioneering SPS studies of InAs/InGaAlAs quantum dashes-in-quantum well (DHWELL) structures for light emitters reported in papers **F3, R1** and **R2**. We have examined the optical properties of these structures and how they are influenced by the interface intermixing, obtained by two different techniques, to tune the emission wavelength toward the optimal value for fibre telecommunication 1.55 μm.

3.2.1. Structures intermixed by the impurity-free vacancy disordering

Experimental details

The samples are InAs/InGaAlAs DHWELL laser structures grown by molecular beam epitaxy[3]. The active region consists of 4 undoped 5 monolayers (ML) thick InAs quantum dash (QDH) layers, each one embedded within a 7.6 nm thick compressively strained $In_{0.64}Ga_{0.16}Al_{0.2}As$ QW with a 15 nm thick tensile strained $In_{0.50}Ga_{0.32}Al_{0.18}As$ barrier (QB) layer (Fig. 3.2.1.). A standard separate confinement heterostructure (SCH) layer consisting of a 160 nm thick undoped $In_{0.52}Ga_{0.28}Al_{0.2}As$ was grown on top of a 200 nm thick Si-doped

[3] The fabrication of the samples, their intermixing, the structural studies and the PL measurements at room temperature were performed at Lehigh University, USA.

($1x10^{18}cm^{-3}$) $In_{0.52}Al_{0.48}As$ cladding layer. Both layers are lattice-matched to the (100) oriented, S-doped (3×10^{18} cm^{-3}), InP substrate. The growth was terminated after the top 160 nm thick SCH layer.

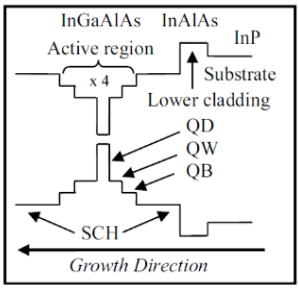

***Figure 3.2.1**. Schematic representation of the band structure of the samples.*

TEM measurements have shown that the QDHs have an average height of 3 to 4 nm and are preferentially elongated along the [$0\bar{1}1$] direction, with length varying from 30 to 60 nm and width in the range of 15–22 nm. For the intermixing process using the impurity-free vacancy disordering (IFVD) technique [21] the samples were firstly coated with 150 nm Si_xN_y as an annealing cap, by using PECVD and then subjected to RTA at 800 ºC in nitrogen ambient for 30 s. The dielectric layer was chemically removed after annealing. The SPS measurements in the soft-contact mode were performed at room temperature with a photon flux density of ~2×10^{14} $cm^{-2}s^{-1}$ and light modulated at 94 Hz. The PL measurements used a 980 nm semiconductor diode laser, a multimode optical fibre and a 0.25 m monochromator with an InGaAs photodetector.

Results and discussion

Since the substrate and the lower cladding layer are heavily n-type doped, while the rest of the structure is nominally undoped, an upwards band bending is present in the structure relative to the substrate. The SPV signal related to the DHWELLs is mainly due to photocarriers that escape via thermal emission and field-assisted tunnelling from the active region towards the SCH layers, where they are separated by the built-in electric field over longer distances – holes move towards the surface, while electrons move towards the substrate. This is evidenced also by the SPV phase (not shown).

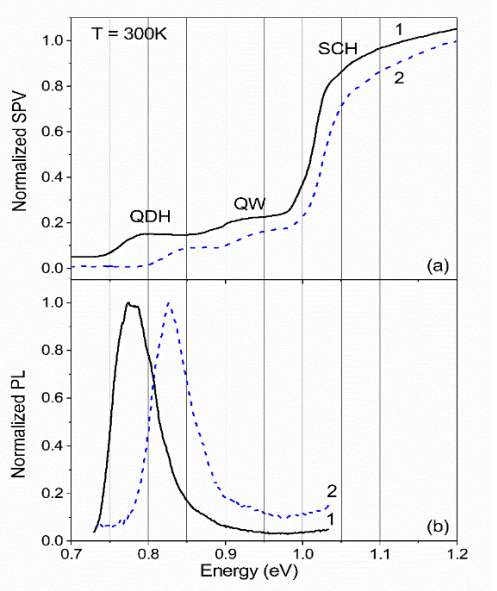

***Figure** 3.2.2. SPV (a) and PL (b) spectra of the as-grown (solid curves) and IFVD interdiffused (dashed curves) InAs/InGaAlAs DHWELL samples. Curve 1 in (a) is vertically shifted for clarity.*

Figure 3.2.2 depicts the room temperature SPV (a) and the PL (b) spectra of the as-grown (curves 1) and interdiffused (curves 2) DHWELL samples. The SPV spectrum reveals step-like features that are related to inter-band optical absorption transitions in the QDH, QW and SCH layers. The PL spectrum only shows a single peak corresponding to the transitions in the QDHs, which have the lowest ground states in the whole structure and offer an effective recombination channel. The large SPV spectral range (~ 58 meV) of step QDH is due to the inhomogeneity of the QDH size distribution, revealed also by TEM and AFM. The SPV spectrum is therefore composed of a series of broad Gaussians [22], corresponding to the QDH ground state as well as excited states optical transitions. It is difficult to resolve the Gaussians corresponding to different transitions, and therefore we observe a step (QDH) rather than peaks in the SPV spectrum related to the QDHs. The inflexion point of this step is taken here as an estimate of the QDH ground state transition energy. The obtained value (0.764 eV) is very close to the PL peak position (0.775 eV).

Curves 2 in Fig. 3.2.2 represent the SPV(a) and the PL (b) spectra of the annealed DHWELL sample. The thermal annealing results in blueshifts of the optical transition energies of the QDH, QW and SCH layers. The shift of the QDH transition energy, determined from the SPV spectra is ~ 52 meV. The bandgap shift determined from the PL spectra is of the same order of magnitude. The blueshift is due to the thermally induced intermixing of group-III atoms (mainly In and Ga) between the InAs QDHs and the surrounding InGaAlAs. The intermixing modifies the compositional profile from an abrupt interface to a graded one resulting in an interfacial graded potential. As a consequence, the potential increases in the InAs QDH region while it decreases in the surrounding InGaAlAs barrier, i.e. the QW region. The first effect pushes the QDH bound state energy levels up, while the second one pushes them down. Since the wave functions of the QDH ground states are localized predominantly in the central part of the QDH, the first effect is stronger. Thus, their energies and therefore the optical transition energy increase, which leads to the observed blueshift of the SPV and PL spectra.

The blueshift of the QW transition energy is ~27 meV. Two interfacial effects influence the potential in the QW: i) the intermixing of the interfaces QW/QDH decreases the potential in the QW layer; ii) the intermixing of the interfaces QW/QB increases the potential in the QW layer. As the QDH volume is smaller than those of the QW and the QB, the second effect is stronger, which results in a blueshift of the QW bound state energy levels and correspondingly to the QW optical transition energy after annealing. The shift value is smaller than that of the QDH transition. This is due to the larger surface-to-volume ratio of the QDHs, which are more influenced by the intermixing-induced changes of the interface potential. The blueshift is further reduced with increasing the volume of the corresponding layer: The SCH transition energy (step SCH) only shifts by ~7 meV, while the InP substrate transition energy (not shown) is unchanged after annealing. Figure 3.2.2 also shows that the intermixing improves the homogeneity of the QDH size distribution. This is evidenced by the narrowing of the SPV step QDH as well as the PL peak in curves 2 as compared to curves 1. The narrowing is the same in both cases (~10-11 %).

3.2.2. Structures intermixed by the nitrogen ion-implantation induced disordering (NIID)

Experimental details

The samples are partial InAs/InGaAlAs DHWELL laser structures grown by MBE, similar to those from the previous section. For the intermixing process using the NIID technique [23], the samples were covered with a 1μm thick SiO_2 layer and the N implantation was performed at room temperature with a dose of $5\times10^{12}cm^{-2}$ and energy of 1500 keV, introducing the peak defect density centre at 0.8 μm below the active region of the structure. This indirect implantation aims to minimize the damage and cluster formations in the active region and possible degradation of the optical properties [24]. The SiO_2 layer was then removed using a buffered oxide etch solution and RTA was performed at 700°C for 2 min with no annealing cap to avoid any possible IFVD effect.

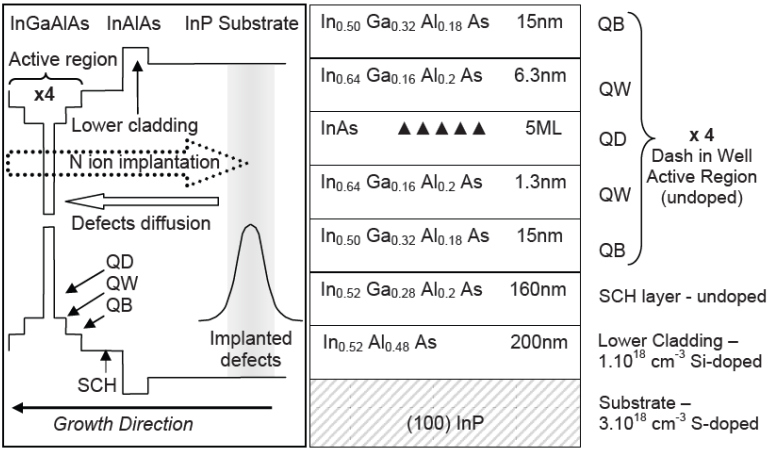

Figure 3.2.3. *Band structure and layer sequence of the InAs/InGaAlAs DHWELL samples. The N implantation process and the diffusion of defects during the annealing are represented with empty arrows.*

The band structure and the layer sequence in the sample are shown in Fig. 3.2.3, which also gives an idea about the N implantation and defect

diffusion. For comparison purposes, we have studied also a control sample annealed under the same conditions, but without ion implantation, as well as an as-grown sample. The SPS and PL measurements were performed as described above with the only distinction of the 532 nm diode-pumped solid-state laser (1.5 $kWcm^{-2}$) used in the PL spectroscopy.

Results and discussion

Figure 3.2.4 presents the SPV and PL spectra of all three samples. The SPV spectra are step-like features composed of a series of broad Gaussians corresponding to the QDH ground state as well as excited states optical transitions. Their energy ranges coincide very well with the positions of the corresponding PL peaks. The energy position of the QDH ground states transitions is in the range of the steep slope of the SPV step, where a weak shoulder can be seen (for the as-grown and control samples). It can be determined more precisely from the position of the corresponding PL peak.

Figure 3.2.4 shows that there is a total blueshift as large as 93 meV (176 nm) between the as-grown and the N-implanted sample, calculated from the SPV step and PL peak positions. It is explained as follows. The N ion implantation introduces vacancies and interstitial defects in the sample, which during the annealing effectively diffuse towards the active region (see Fig. 3.2.3) to enhance the thermally induced intermixing [24]. The intermixing of group-III atoms (mainly In and Ga) between the InAs QDHs and the surrounding InGaAlAs QW modifies the compositional profile from an abrupt interface to a graded one, resulting in an interfacial graded potential. This leads to a blueshift of the bound states and the corresponding transition energies, as explained in Sect. 3.2.2.2. For comparison, the blueshift of the control sample is only 41 meV (80 nm) because the intermixing in this case is due simply to grown-in defects diffusion during the annealing process. The net effect of N implantation is seen from the comparison between the spectra of the control and the N-implanted samples – the differential bandgap shift is also significant, namely 52 meV (96 nm), which proves again the role of the implantation-induced defects in the intermixing process. It should be noted that the same amount of blueshift (52meV) is obtained for the similar samples processed with the IFVD technique employing a 100°C higher annealing temperature, as described in Sect. 3.2.2.2.

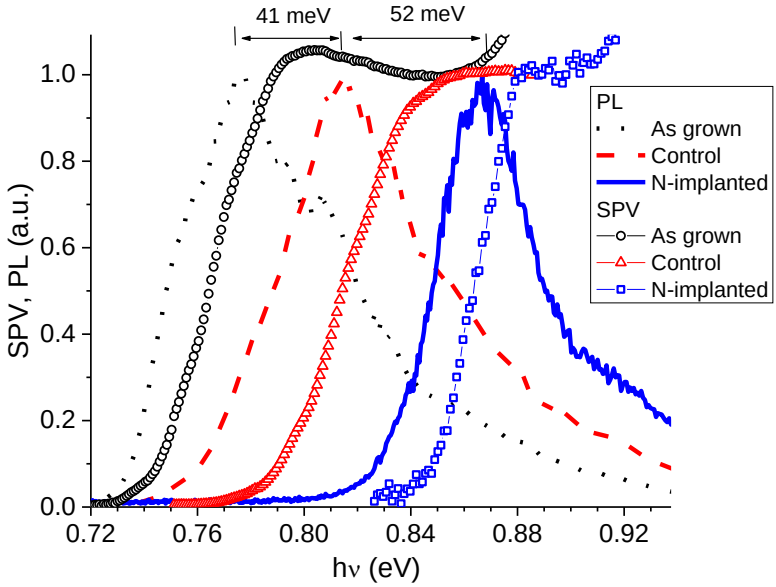

Figure 3.2.4. *SPV (lines& symbols) and PL (lines) of as-grown, control and N-implanted InAs/InGaAlAs DHWELL samples.*

The comparison of the spectra of the control and the N-implanted samples in Fig. 3.2.4 shows that the N implantation also leads to step narrowing in the SPV spectrum (approximately 50%) as well as to PL linewidth reduction (approximately 40%) in agreement with the results in [24]. This is due to the improved homogeneity of the QDH size distribution during the intermixing. Another possible reason for this narrowing could be the fact that after the intermixing the QDH bound states become closer in energy as the potential well of the QDH becomes shallower. This does not allow to resolve the Gaussians corresponding to the ground and excited states transitions, which results in a smoother SPV step of the N-implanted sample revealing no shoulders (contrary to the SPV spectra of the other two samples).

3.2.3. Conclusions

SPS has provided information about the inter-band optical transition energies in all relevant layers of the InAs/InGaAlAs DHWELL structures, including the QDHs, QWs, and SCH layers. The blue shift of these energies as a result of the interface potential grading caused by the intermixing of the material components is also well revealed. It is the largest for the QDHs due to their large surface-to-volume ratio. Employing the NIID technique has resulted in a larger blue shift as compared to the IFVD technique, even using lower annealing temperatures.

3.3. InAs quantum dot-in-quantum well structures for infra-red photodetectors

The QD infra-red photodetectors (IRPDs) are based on inter-subband transitions in self-assembled InAs QDs. They have several advantages over QW-based IRPDs such as the possibility of detecting normally incident light, lower temperature sensitivity, increased carrier lifetimes and lower dark current. Despite these advantages, they face some technical problems such as difficulties in achieving QD size and shape uniformity, as well as large density arrays of QDs with smaller QD sizes. Solutions to these problems are sought in growing i) QDs in quantum well (DWELL) structures and ii) multi stacks of submonolayer QDs or both. This section presents our pioneering SPS studies reported in paper **F9** of the inter-band optical transitions and the photocarrier transport in two types of DWELL structures designed for IRPDs. The first structures contain InAs/GaAs submonolayer QDs, while in the second structures the QDs are grown by the Stranski-Krastanov mode.

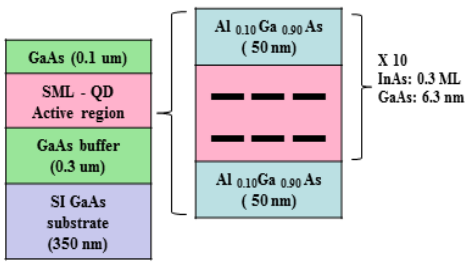

Figure 3.3.1. *Layer sequence of sample 3002 containing submonolayer InAs QDs schematically represented as black rectangles.*

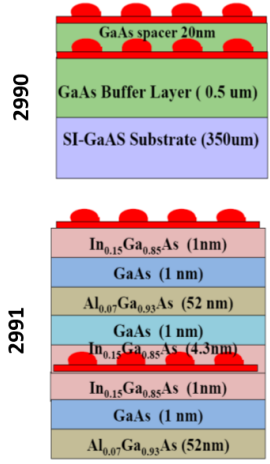

Figure 3.3.2. *Layer sequences of samples 2990 and 2991 containing Stranski-Krastanov QDs.*

3.3.1. Experimental details

Two series each including two samples grown on semi-insulating GaAs substrates are studied[4]. In the first series (Fig.3.3.1.), referred to as SML-QD (samples 3001 and 3002) the active region consists of ten periods of GaAs QWs (6.3 nm) with AlGaAs barriers (50 nm). In sample 3002 submonolayer (SML) InAs QDs (0.3 monolayers) are embedded in the GaAs QWs. Sample 3001 has no QDs and is used for comparison. In the samples from the second series (Fig. 3.3.2), referred to as SK-QD (samples 2990 and 2991) there are two QD layers grown by the standard Stranski-Krastanov mode. In sample 2990 the QD layers are separated by a 20 nm GaAs layer, while in sample 2991 the lower QD layer is embedded in a double QW of InGaAs/GaAs/AlGaAs.

The SPS measurements in the soft-contact mode were performed at room temperature with a photon flux density of 1.5×10^{14} $cm^{-2}s^{-1}$ and light modulated at 94 Hz and 469 Hz. PL was measured using a He-Ne laser and an InGaAs detector.

3.3.2. Results and discussions

Because of the residual p-type doping (~ $10^{15}cm^{-3}$), SCR develops at the surface with energy bands bent downwards relative to the bulk and an electric field directed from the surface to the bulk. The width of the SCR is assessed to be around 900 nm, therefore the epitaxial structure in both series of samples is in the SCR.

3.3.2.1. Series SML-QD (submonolayer QDs)

Figure 3.3.3 presents the SPV amplitude and phase spectra of both SML samples measured at 469 Hz. In sample 3001 (Fig.3.3.3 (a)) there are no QDs, hence all spectral features in the energy range 1.0 – 1.42 eV originate from optical transitions in the SI GaAs substrate. The obtained information is used for comparison in the analysis of the results from the other samples. The smooth increase in the SPV amplitude in the range 1.0 – 1.30 eV with phase values in the IInd quadrant indicates domination of electronic transitions between the CB

[4] The samples were grown by MBE at the University of New Mexico, USA, where also the PL measurements were done.

and deep levels resulting in free holes and captured electrons. At higher photon energies $h\nu$ two sharp peaks appear at 1.38 eV (with a phase in the IInd quadrant) and 1.40 eV (with a phase in the IVth quadrant), respectively followed by a plateau above 1.42 eV. In agreement with the discussion in [25], the peak at 1.38 eV is ascribed to electronic transitions between the VB and shallow traps near the CB of SI GaAs resulting in free holes and captured electrons, while the peak at 1.40 eV is attributed to transitions between shallow acceptors and the CB generating free electrons and captured holes. Thus, the sharp phase change from IInd to IVth quadrant in the range 1.35 – 1.40 eV is explained by the change of the dominant SPV process. The arrow in Fig. 3.3.3 (a) marks the position of the PL peak of sample 3001. It coincides in energy with the SPV peak at 1.38 eV. The transitions corresponding to the SPV peak at 1.40 eV are not active in the PL, because the shallow acceptors are filled with electrons at room temperature.

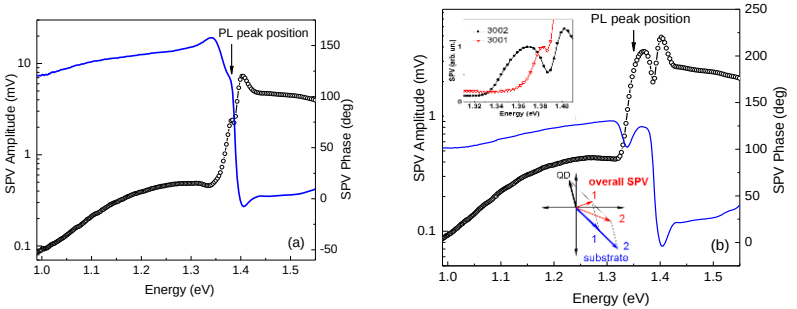

Figure 3.3.3. *SPV amplitude (symbols) and phase (lines) spectra of samples 3001 (a) and 3002 (b) measured at 469 Hz. The arrows mark the positions of the PL peaks. In (b) the lower inset represents a vector diagram showing the interaction of the SPV processes related to the QDs and the substrate in the range 1.37 - 1.40 eV. The upper inset compares the SPV amplitude spectra of the two samples.*

The SPV amplitude and phase spectra of sample 3002 with SML QDs measured at 469 Hz are shown in Fig. 3.3.3 (b). Below 1.30 eV the spectra are similar to the spectra of the previous sample and originate from deep level related transitions in the substrate. Above 1.31 eV the phase begins to decrease towards 0^{o}, which is due to the tail of the transitions between shallow acceptors and the CB, as observed in sample 3001. However, at 1.34 eV it increases again to form a peak of 140^{o} at 1.37 eV. The SPV amplitude spectrum reveals a step

in the range of 1.33 eV - 1.37 eV. It corresponds well to the position of the PL peak at 1.35 eV (not shown) marked with an arrow in Fig. 3.3.3 (b). This allows us to ascribe the SPV process in the range 1.33 eV - 1.37 eV to optical transitions between the ground electron and hole states of the SML QDs. The SPV signal is due to photocarriers, which thermally escape from the QDs into the GaAs QWs and AlGaAs barriers, where they are separated by the built-in electric field of the SCR. Considering the direction of the electric field mentioned above, the electrons move towards the surface and the holes ─ towards the bulk resulting in an SPV phase in the IInd quadrant. Carrier capture and reemission processes by the potential wells (QDs and/or QWs) of the next layers are also possible.

To better demonstrate the contribution from the QDs the upper inset of Fig. 3.3.3 (b) compares the SPV amplitude spectra of samples 3002 (with QDs) and 3001 (without QDs). It is seen that the presence of QDs substantially modifies the spectrum by shifting the absorption edge towards lower energies. The SPV process related to the QDs dominates in the range 1.33 - 1.37 eV.

Immediately after the step related to the SML QDs in Fig. 3.3.3 (b) one observes a decrease in the SPV amplitude and a sharp jump of the SPV phase from the IInd to the IVth quadrant. This is due to the inclusion of the above discussed SPV process with a phase in the IVth quadrant originating from the transitions between shallow acceptors and the CB in the SI GaAs substrate. The appearance of a vector in the IVth quadrant decreases the magnitude of the overall SPV vector and rotates it clockwise as illustrated by the vector diagram in the lower inset in Fig. 3.3.3 (b). Considering all this we note that the SPV peak at 1.37 eV is an artefact due to the combination of two SPV processes and therefore its position should not be compared to the PL peak position.

3.3.2.2. Series SK-QD (Stranski-Krastanov QDs)

Figure 3.3.4 (a) displays the SPV spectra of sample 2990 (containing InAs/GaAs SK QDs) measured at 94 Hz. The background in the SPV amplitude for $h\nu < 1.30$ eV is dominated by transitions between deep levels and the CB in SI GaAs resulting in an SPV phase in the IVth quadrant. In the range 1.00 - 1.16 eV one observes two steps in the amplitude spectrum and a continuous change of the phase towards 0°. This range corresponds to the energy positions of the PL peak at 1.04 eV and its shoulder at 1.12 eV (not shown) marked with arrows in Fig. 3.3.4 (a). Therefore, these SPV features are attributed to optical transitions between QD states. Considering that the QD transitions result in an SPV vector in the IInd quadrant, while the dominant deep level related process

in this range has a phase in the IVth quadrant, the inclusion of the QD processes should decrease the SPV amplitude and change the SPV phase towards the IInd quadrant. Therefore, the QD-associated transitions are manifested as small dips rather than peaks in the SPV amplitude spectrum. The dip at 1.06 eV is ascribed to transitions between electron and hole ground states, while that at 1.14 eV – to transitions between excited states. Compared with the PL features these transitions are at slightly higher energies (20 meV), which is the Stokes shift between absorption (SPV) and emission (PL). The energy spacing between ground and excited states transition energies is however the same in both cases (80 meV). The photogenerated electrons and holes thermally escape from the QD into the GaAs layers where they are separated by the built-in electric field of the SCR. The electrons move towards the surface some 20 nm, which is the thickness of the GaAs spacer. The holes move towards the bulk inside the GaAs buffer layer over longer distances. Therefore, the hole drift towards the substrate is the main mechanism of carrier separation in the SPV generation in this case.

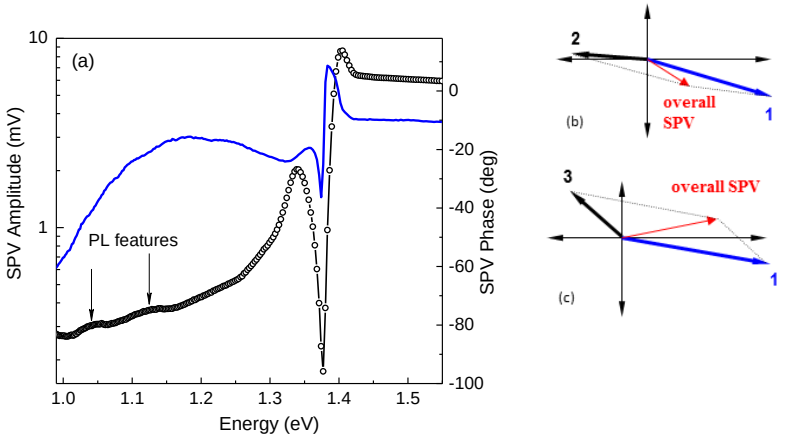

Figure 3.3.4. *(a) SPV amplitude (symbols) and phase (line) spectra of sample 2990 (containing InAs SK QDs in GaAs), measured at 94 Hz. The arrows mark the positions of the PL peak and its high-energy shoulder. (b) and (c) Vector diagrams showing the interaction of different SPV processes in the range 1.35 – 1.37(4) eV (b), and 1.37(4) – 1.38(4) eV (c) (see text).*

Above 1.30 eV the SPV amplitude increases faster. However, between 1.34 eV and 1.40 eV, it reveals a sharp and deep minimum at 1.37 eV, while the phase shows a dip at 1.37 eV and then a positive peak at 1.38 eV. This strange behaviour is explained with the help of the vector diagrams in Figs. 3.3.4 (b) and (c). The process marked as vector 1 in the IVth quadrant is due to the transitions between shallow acceptors and the CB in the substrate. As mentioned above, it starts already at around 1.30 eV. The appearance of vector 2 (with an obtuse angle with vector 1 oriented downwards) leads to the sharp amplitude and phase minima at 1.37 eV. It is ascribed to optical transitions between the electron and hole ground states in the wetting layer in agreement with photocurrent spectroscopy results [26]. The appearance of vector 3 (with an obtuse angle with vector 1 oriented upwards) rotates the overall SPV vector anti-clockwise forcing its phase to shortly enter the Ist quadrant revealing the peak at 1.38 eV. It is ascribed to transitions between the VB and shallow traps near the CB in the substrate, as discussed for sample 3001. At higher $h\nu$ process 1 dominates leading to the amplitude peak at 1.40 eV and phase values in the IVth quadrant above 1.42 eV.

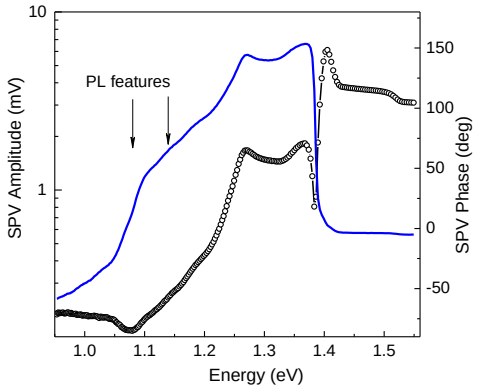

Figure 3.3.5*. SPV amplitude (symbols) and phase (line) spectra of sample 2991, measured at 94 Hz. The arrows mark the positions of the PL peak and its high-energy shoulder.*

The SPV spectra of sample 2991 containing DWELL measured at 94 Hz are presented in Fig. 3.3.5. Below 1.05 eV the SPV phase is in the IVth quadrant

indicating again domination of transitions between deep levels and the CB. However, in the range 1.05 – 1.10 eV it quickly changes anti-clockwise to the Ist quadrant revealing a step with an inflection point at 1.08 eV. Such behaviour indicates the inclusion of an SPV process in the IInd quadrant corresponding to electron (hole) movement towards the surface (bulk). Therefore, it originates from the SCR. In the same range, a negative bump (a minimum) is observed in the SPV amplitude spectrum centred also at 1.08 eV. The positions of the PL peak (1.08 eV) and its shoulder (1.14 eV) are marked with arrows Fig. 3.3.5. Having in mind the coincidence with the PL peak energy we ascribe the observed SPV features in the range 1.05 –1.10 eV to optical transitions between the ground electron and hole states in the QDs. As in the case of sample 2990, the inclusion of the QD process decreases the SPV amplitude and changes the SPV phase anti-clockwise towards the IInd quadrant. Again, due to the sample geometry, the hole drift towards the bulk is over longer distances than the electron drift towards the surface and therefore is the dominant carrier separation process.

At higher energies, one observes a peak at 1.27 eV in the SPV amplitude and in the SPV phase in the IInd quadrant, which is ascribed to electronic transitions between the ground states in the $In_{0.15}GaAs_{0.85}$/GaAs QW. After 1.37 eV the phase jumps into the IVth quadrant, while the amplitude reveals a sharp minimum at 1.38 eV and increases again to form a peak at 1.40 eV. This behaviour is again explained by the inclusion of the above-discussed transitions (at 1.40 eV) in the substrate between shallow acceptors and the CB. The addition of the corresponding SPV vectors is similar to the scheme shown in the inset of Fig. 3.3.3 (b).

Finally, we compare the SPV signal generated from QD transitions in the two series of samples. The SK QDs (samples 2990 and 2991) show lower transition energies and much lower SPV signals than the SML QDs (sample 3002). The lower transition energies result from the lower bound state energies in the InAs/(In)GaAs potential well, which are due to the larger size of the SK QDs. One of the reasons for the smaller signal is the different number of QD layers in the two series (10 in SML-QDs vs 2 in SK-QD). However, the observed signal difference is more than 10 times. Therefore, there is another reason for this result and it is related to the different carrier escape probability from the QDs. The lower energies of the bound states in the SK QDs lead to a lower escape probability of the generated photocarriers and this way lower SPV signal.

It is worth noting however that the low escape probability in the SK QDs is an advantage for QD IRPDs applications because it contributes to achieving lower dark current.

3.3.3. Conclusions

Using SPS and PL we have determined the energies of the QD related transitions in complex DWELL nanostructures containing InAs SML QDs and InAs SK QDs prospective for IR photodetectors. SK QDs reveal lower SPV signals and lower transition energies, which is explained in terms of their larger size. Hole drift towards the bulk is the main mechanism for carrier separation and transport in the SPV generation process in these structures. The SI GaAs substrate has a substantial contribution to the SPV spectra. The interaction of its SPV signal with the signals from the nanostructure results in non-trivial SPV spectral features. They were successfully explained by the vector model, which highlights its potential for retrieving information about different superimposed SPV processes.

3.4. Multi-layer structures with InP/GaAs type-II quantum dots

The InP/GaAs quantum dots (QDs) are type II heterostructures, where the electron is confined in the InP material while the hole remains in the GaAs layer around the QDs, due to the Coulomb attraction. The spatial separation of the carriers results in a weaker exciton binding energy as compared to the type I QD exciton. The electron-hole wave function spatial overlap is also much smaller for type-II QDs, resulting in relatively long carrier lifetimes. Due to these properties and their near-infrared (~0.95 μm) optical transition energies, InP/GaAs QDs are promising candidates for optical memories and optical communication devices. They are more complex systems as compared to type I QDs, because of the different possibilities for hole wave function distribution around the QD, which is very sensitive to the QD geometry. The study of multi-layer type II QDs is further complicated, because of the structural and electronic couplings between dots adjacent along the growth direction, which depends on the spacer layer parameters.

This section presents our pioneering study on multi-layer structures with InP/GaAs type-II quantum dots as reported in papers **F7-F8**. At the time when the study was carried out the published works devoted to the optical properties of InP/GaAs QDs were mainly based on PL measurements. Few results were available in the literature concerning the optical absorption of type II QD systems. As an alternative to the optical absorption, we have used the high-sensitive SPS. The measurements were done at liquid nitrogen temperature (73 K) which allowed direct comparison with PL results, bearing in mind that no PL signal was detected at room temperature.

3.4.1. Experimental details

The self-assembled InP/GaAs QDs were grown by the Stranski-Krastanov mode in a chemical beam epitaxy (CBE) system[5]. The sample contains 10 periods of InP/GaAs QDs layers separated by GaAs spacer layers with a nominal thickness of 5 nm. The top QD layer was left uncovered to perform AFM measurements. The structure is grown on a 300 nm GaAs buffer

[5] The sample growth and structural characterization were done at Campinas University, Brazil

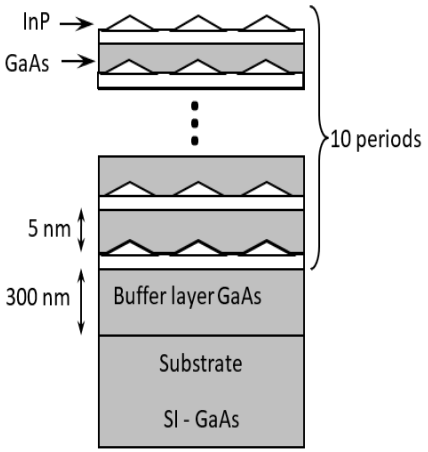

Figure 3.4.1. *Layer sequence in the InP/GaAs QD sample*

layer deposited on a (001) oriented semi-insulating (SI) GaAs substrate. A schematic of the sample structure is shown in Fig. 3.4.1. The multi-layer structure and GaAs buffer layer reveal p-type residual doping of around 10^{16}cm^{-3}. PL measurements were performed by the author during his research stay at Campinas University using a 200 mW diode laser (532 nm), a SPEX single grating monochromator (1200gr/mm) and an N_2 cooled Ge detector connected to a Lock-in amplifier. SPV spectra were recorded using the SPV set-up and measurements procedure described in Sect. 2.1.

3.4.2. Results and discussion

AFM measurements have revealed an average QD height of (3.2±0.9) nm, an average radius of (18±3) nm and a dot density of 3.5×10^{10} cm^{-2}. TEM image has shown that the QDs in the first layer are smaller than the thickness of the GaAs spacer layer, thus these QDs are physically separated from the next InP layer. However, this separation decreases for the subsequent layers and the dots after the fourth layer coalesce into a quantum post (QP)-like structure [27,28].

Typical SPV amplitude and phase spectra of the QD sample, measured at 73 K, are presented in Fig. 3.4.2. To facilitate the analysis, they can be divided into two parts: a low-energy range for photon energies $h\nu < 1.38$ eV and a high-energy one for $h\nu > 1.38$ eV.

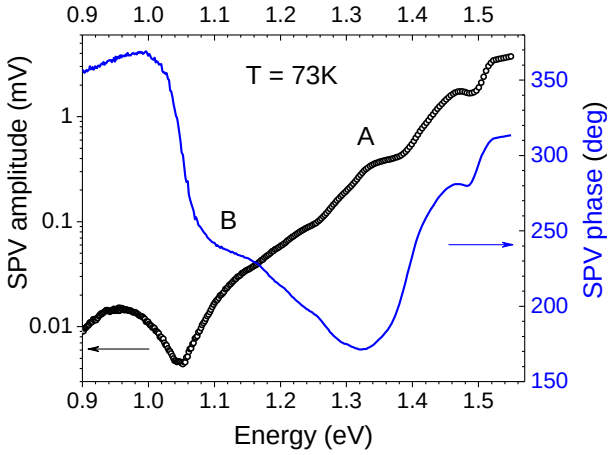

Figure 3.4.2. *SPV amplitude (symbols and left scale) and phase (solid line and right scale) spectra of the InP/GaAs QD sample, measured at 73 K.*

Low-energy range (hν < 1.38 eV) of the SPV spectra

Due to the p-type residual doping of the multi-layer structure and buffer layer, the energy bands at the surface are bent downward compared to the bulk. Thus, the QD structure and a part of the GaAs buffer layer are situated in the surface SCR, which thickness is assessed to be ~215 nm [27].

For hν < 1.0 eV the SPV signal is due to optical transitions related to deep levels (DL) in the SI GaAs substrate. The SPV phase is near 360°, indicating a predominant movement of free electrons towards the bulk or/and holes toward the surface.

In the range 1.0 < hν < 1.16 eV the SPV amplitude reveals a minimum at 1.05 eV, while the SPV phase drastically changes clockwise by more than 100° and approaches 240°. Such SPV behaviour corresponds to the appearance and increase of a new SPV process with a phase in the IInd quadrant close to 180°, which is superimposed to the DL-related process. This is explained using the vector diagram in Fig. 3.4.3, where the SPV vectors of this new process and that of the DL-related process are labelled QP and DL, respectively. Two

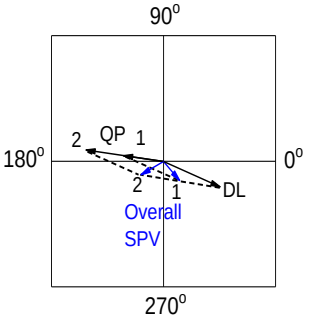

Figure 3.4.3. *Vector diagram representing the SPV processes for 1.0 < hν < 1.16 eV.*

consecutive states of the QP and the overall SPV vectors are shown and labelled "1" and "2". The vector QP increases with increasing hν, forming an obtuse angle with vector DL. As a result, the overall SPV vector rotates clockwise, while its magnitude reveals a minimum at hν = 1.05 eV. The phase of the new SPV process indicates hole movement towards the substrate and/or electron movement towards the surface, which is due to the downward band bending in the QD structure. This implies that the new SPV process originates from the QD structure. Its signal overcomes the signal from the DL transitions and leads to the step in the amplitude spectrum in the range 1.05–1.16 eV. Further on, this step is labelled "B".

For hν > 1.16 eV the SPV amplitude continuously increases and reveals another step in the range 1.25–1.38eV labelled "A". At the same time, the SPV phase continues its change in the clockwise direction, forming a minimum at 1.32 eV. In terms of the vector model, this behaviour is explained by the appearance and increase of another SPV vector in the IInd quadrant, which is added to the above-depicted vectors. This new vector should have an orientation similar to that of the QP vector [27]. The amplitude and phase of the SPV process, corresponding to step A, implies that it takes place in the QD structure where the energy bands are bent downward. Its magnitude is larger as compared to the process, corresponding to step B.

To assess the possible influence of the SPV generated in the SI GaAs substrate in the range 1.0 - 1.38 eV, we have measured the SPV spectrum at 73K of a bare substrate sample. In this range the SPV amplitude and phase exhibit no distinct spectral features, revealing a different behaviour as compared to the spectra of the QD sample from Fig. 3.4.3.

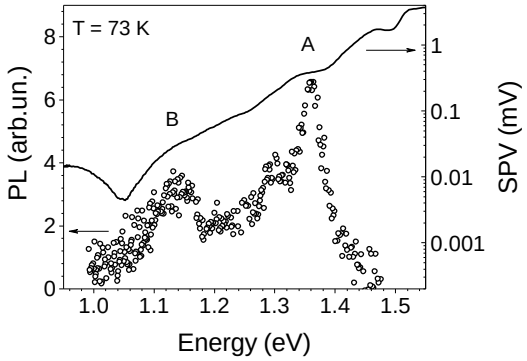

Figure 3.4.4. *The photoluminescence spectrum (open circles) of the QD sample measured at 73 K with an excitation density of 3 Wcm^{-2}. The SPV amplitude spectrum (solid line) from Fig. 3.4.2 is added for comparison.*

Figure 3.4.4. presents the PL spectrum of the same sample measured at 73 K for comparison purposes. As we could not detect PL with an excitation density as low as that used in the SPV experiment we have used one of the lowest possible excitation densities (3 Wcm^{-2}) which gives a reasonable PL signal. In the range of 1.05 - 1.18 eV the PL spectrum shows a broad band, labelled B, centred at 1.14 eV, while at higher energies it reveals a sharp peak at 1.36 eV, labelled A. These energies fall within the spectral ranges of the SPV steps B and A, respectively.

The good correspondence in energy positions of bands A and B in the SPV and PL spectra allows concluding that they are due to optical transitions between the same energy states. The origin of the PL bands A and B was determined in [28] where we performed a detailed PL study at 10 K on the same multi-layer InP/GaAs QD sample using different excitation intensities. Following the discussion given in [28], we ascribe the SPV band B to electronic transitions from the valence band (VB) states in the GaAs spacers to the conduction band (CB) states in the InP QPs, while the SPV band A is attributed to similar transitions, but involving the CB states of the wetting layer (WL), as illustrated in Fig. 3.4.5.

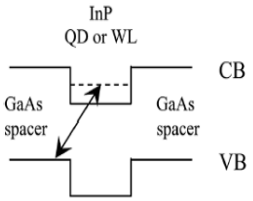

Figure 3.4.5. *Schema of the energy band line-up and electronic transitions in one period of the multi-layer InP/GaAs QD structure.*

The energy of PL band B (1.14 eV) is considerably lower (by 180 meV) than the emission energy (1.32eV) of single-layer capped InP/GaAs QDs observed at 7K [29]. The temperature-related red shift for this band from 7 K to 73 K is only 56 meV, as found from the comparison of the PL spectra in [27] and [28] recorded at the same excitation intensity. Therefore, the lower energy position of band B is mostly due to the vertical coupling of the QDs forming QPs with a size much larger as compared to the single QDs. The PL peak energy of band A (1.36eV) is also lower than the energies (~1.41–1.45 eV) observed for WL emission at 10 K in single layer InP/GaAs QDs [30], the difference being ~52 meV. The temperature-related red shift from 10 K to 73 K for this band is only 13 meV [27,28]. Consequently, the main reason for the lower energy of the WL absorption/emission (band A) is connected with the electronic coupling effect between the WL planes in the here investigated multi-layers with relatively thin GaAs spacers.

Mechanisms of carrier separation in space

To clarify the main mechanisms of photocarrier separation in space that gives rise to SPV we consider the following: i) The phase of the SPV signals from the QPs and WL is in the IInd quadrant, which implies that photogenerated holes (electrons) predominantly move towards the substrate (surface); ii) To leave the QD structure and move towards the substrate, the electrons from the InP QPs have to overcome the barrier formed by the smaller QDs in the first 1-3 layers, as well as the barrier of the GaAs buffer layers; iii) The holes, generated in the GaAs spacer layers, have much more freedom to move towards the substrate because the InP barriers of the WL are very thin and no additional barrier between the structure and the GaAs buffer layer exists; iv) The SCR electric field favours the hole movement towards the substrate and impedes the electron movement in this direction; iv) As the QD structure is very thin (~ 40

nm), the holes cover much longer distances (including part of the GaAs buffer layer) than the electrons.

Considering the above discussion, we can conclude that the main mechanisms of carrier separation include hole drift and diffusion towards the substrate. A smaller contribution is the electron drift towards the surface. These mechanisms give rise to an SPV signal from the QP structure with a phase in the IInd quadrant, which is superimposed on the DL-related signal. The superposition of the two signals leads to the observed SPV signal with phase in the IIIrd and IInd quadrants in the low-energy range of the spectrum.

High-energy range ($h\nu$ > 1.38 eV) of the SPV spectra

Above 1.38 eV the SPV behaviour can be explained by the consecutive appearance of two SPV processes in bulk GaAs with phases in the IVth quadrant as follows. Having in mind the ionization energy of the Si shallow acceptor in GaAs (34 meV) the peak at 1.47 eV is attributed to transitions between shallow acceptors and the CB in the substrate. They provide free electrons and trapped holes leading to an SPV vector in the IVth quadrant. At higher energies, the 1.508 eV step in the SPV spectra originates from the band-to-band free carrier generation in the SI GaAs substrate, which is a strong and fast process with a phase in the IVth quadrant closer to 360° due to the Dember effect. These two processes rotate the overall SPV vector from the IInd through the IIIrd towards the IVth quadrant, as observed in Fig. 3.4.2.

3.4.3. Conclusions

The optical transitions related to the QDs and the WLs are revealed as two well-separated spectral bands in the SPV and PL spectra of multi-layer self-assembled InP/GaAs type-II QDs. Electronic coupling between the layers and vertical coalescence of large QDs into quantum posts is observed. Hole drift and diffusion from the QD structure towards the substrate is the main mechanism of photocarrier separation in space. The absorption in the SI GaAs substrate dominates the SPV spectra for energies below 1.0 eV and above 1.38 eV.

CHAPTER 4. SPS of MATERIALS for PHOTOVOLTAICS

4.1. Silicon nanowires prepared by metal-assisted chemical etching

Silicon nanowires (SiNWs) fabricated by metal-assisted chemical etching (MACE) [31] constitute a material of very low reflectance (below 2-3%), which is prospective for light trapping on the front surface of a c-Si solar cell [32]. To implement this type of SiNWs in a c-Si solar cell, one of the main issues is carrier recombination at the very large SiNW surface, part of which is due to structural defects at the SiNW surface, which should be reduced to a minimum by implementing suitable methods. In this section, we describe our SPS studies reported in paper **F10** aiming to assess the effectiveness of the chemical treatment applied after the MACE process in reducing recombination centres at the SiNW surface and get an additional insight into the SiNW properties. At the time when our work was conducted, it was one of the first SPS studies on SiNWs prepared by the MACE process.

4.1.1. Experimental details

The experimental samples[6] were prepared using p-type (100)-oriented Si wafers with a resistivity of 1-2 Ω.cm. A single-step MACE process was applied for the SiNW formation, as described in [31]. After etching, the samples were dipped in 50% HNO_3 to completely dissolve the Ag dendrites and any other Ag residues from the SiNW surface. Consequently, the samples were subjected to chemical treatment with HF/piranha (mixture of H_2SO_4 and H_2O_2)/HF to remove structural defects from their surface, which result from the etching process. In the following, as-grown SiNW samples without any chemical treatment are referred to as p-a, while p-b (p-c) are respectively samples with a single (double) cycle of HF/piranha/HF cleaning. For comparison, reference p-Si substrate samples, denoted p-sub, were also studied.

Two series of SPV spectra were recorded – one with high photon flux density ($\approx 10^{14}$ $cm^{-2}s^{-1}$) and one with sufficiently lower photon flux density ($< 10^{13}$ $cm^{-2}s^{-1}$) so as the dependence of the SPV on it becomes (nearly) linear.

[6] The fabrication of the samples and their chemical treatment was done in the National Centre of Scientific Research "Demokritos", Athens, Greece.

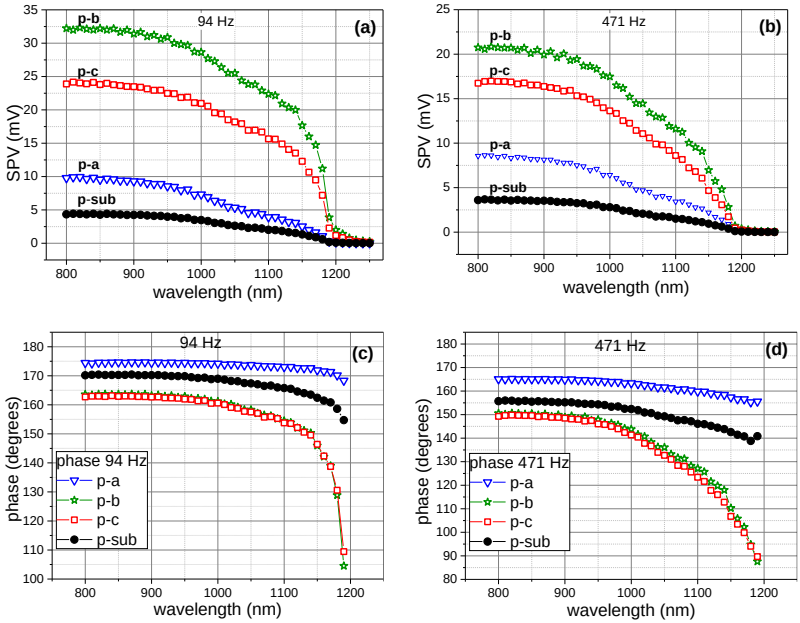

Figure 4.1.1*. SPV amplitude (a,b) and phase (c,d) spectra of all SiNW samples, measured with high photon flux density at 94 Hz (a,c) and 471 Hz (b,d).*

4.1.2. SPS measurements with high photon flux density

Figure 4.1.1 presents the SPV amplitude and phase spectra recorded in all studied samples at 94 Hz and 471 Hz. All SPV amplitude spectra reveal a similar shape including a weakly expressed shoulder in the range of 1050 –1200 nm, which is called low-energy spectral structure (LES), followed by another step in the range 800-1050 nm, called high-energy spectral structure (HES). The SPV phase is in the IInd quadrant for all samples, indicating a downward energy band bending in the direction towards the surface, in agreement with the p-type doping [4,11]. However, its values are different for different samples and also vary with light wavelength and modulation frequency.

In the analysis of the SPV spectra, we bear in mind that the SPV amplitude increases with the increase of the optical absorption coefficient α, the effective carrier lifetime τ_{eff} and the distance Δx over which the photogenerated electrons and holes are separated by the SCR electric field. For downward band bending the phase delay is given by $\Delta\varphi = 180^{o} - \varphi$.

The HES is ascribed to band-to-band transitions having in mind its spectral range and its phase close to 180°. The LES in the **substrate** is attributed to electron transitions between shallow B acceptors (ionization energy of 45 meV) and the CB followed by thermal repopulation of the acceptor levels with electrons from the VB. Such a mechanism of SPV generation is slower than band-to-band transitions, which explains the larger phase delay $\Delta\varphi$ of the LES as compared to the HES.

For **sample p-a**, both HES and LES reveal smaller phase delays as compared to the substrate (see Fig. 4.1.1 (c), (d)) i.e. the corresponding processes are faster. This is explained by the nano-roughness and structural defects at the as-grown SiNW surface, which introduce a high density of surface states (SS). These states increase the surface recombination velocity thus decreasing the effective carrier lifetime, τ_{eff}, given by $1/\tau_{eff} = 1/\tau_{bulk} + 1/\tau_{surf}$. As a result, the carrier generation-recombination processes become faster, leading to a smaller $\Delta\varphi$ of the SPV signal. Concerning the SPV amplitude, we can distinguish two effects of the SS with opposite consequences. The first one is related to the decreased τ_{eff}, resulting in smaller SPV amplitude. However, the SPV amplitude observed in sample p-a is larger than that of the substrate. This is explained by an increased downward band bending at the surface in sample p-a due to positively charged SS, which results in larger surface SCR, i.e. larger Δx, and correspondingly larger SPV. This second effect of the SS on the SPV amplitude dominates in sample p-a.

Sample p-b shows larger phase retardation, i.e. slower processes than samples p-a and p-sub for both HES and LES (Fig. 4.1.1 (c), (d)). This is attributed to reduced surface recombination velocity (increased τ_{eff}) as a result of the reduced density of SS after the HF/Piranha/HF chemical treatment. The SPV amplitude for sample p-b is higher than for sample p-a (Fig. 4.1.1. (a), (b)). To explain this, we have to consider again the two opposite effects of the SS.

Lower SS density results on the one hand in increased τ_{eff}, and on the other hand – in lower energy band bending, i.e. narrower SCR and smaller Δx. The increased SPV amplitude and phase delay show that the contribution of the first factor (increased τ_{eff},) is larger in sample p-b contrary to sample p-a. This leads to the conclusion that a substantial reduction of SS density is already achieved with the first chemical treatment.

The **samples p-c** and p-b have very close SPV phase values (Figs. 4.1.1 (c), (d)). This is explained by their similar values of τ_{eff} (see below). The SPV amplitude of sample p-c is lower than that of sample p-b (Figure 4.1.1 (a), (b)). This is attributed to smaller Δx as a result of further reduction of SS density. This effect dominates over the reduction of SS recombination velocity.

4.1.3. SPS measurements with low photon flux density

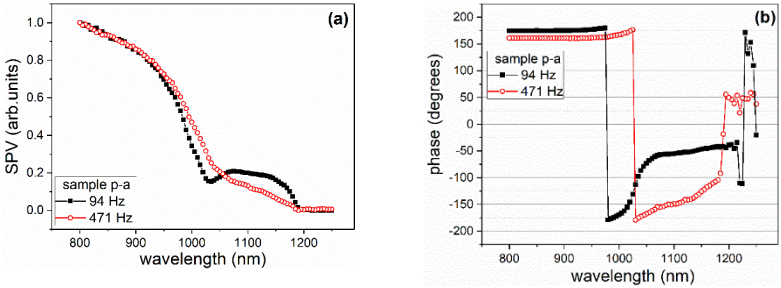

Figure 4.1.2*. SPV amplitude (a) and phase (b) spectra of sample p-a measured with low photon flux at 94 Hz (full black squares) and 471 Hz (open red circles). In (a) the spectra are normalized to unity.*

The SPV spectra of sample p-a recorded at low flux density are shown in Fig. 4.1.2. At 94 Hz the amplitude reveals a new feature - a broad bump in the LES with phase in the IVth quadrant. The corresponding process interacts with the band-to-band transitions (the tail of the HES) leading to an amplitude minimum around 1030 nm because of the nearly opposite phases. The contribution of this strange process is strongly reduced at high frequency and

does not appear in the spectra of samples p-b and p-c (not shown). This suggests that it is a relatively slow surface-related process that is reduced by the chemical treatment. A tentative explanation is proposed including transitions from SS near the VB to the CB followed by diffusion of photogenerated electrons towards the bulk against the SCR electric field.

Minority carrier diffusion length

SPV measurements with low photon flux were used to assess the minority carrier diffusion length, *L*, in the samples under study. The method called "Constant magnitude surface photovoltage" or "method A" was applied observing all requirements needed [33]. It consists of keeping the SPV constant for several wavelengths λ by changing the photon flux density Φ. By plotting $\Phi(\lambda)$ as a function of $1/\alpha(\lambda)$ a straight line is obtained, which intercepts the abscissa at *-L*. Figure 4.1.3 shows the obtained value for sample p-a under excitation at 94 Hz, while the results for all samples at both frequencies are summarized in Table 4.1.1.

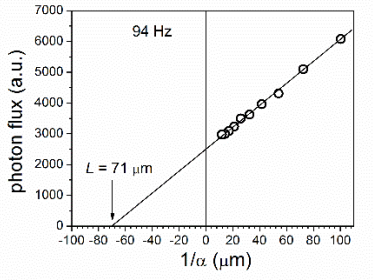

***Figure 4.1.3**. Photon flux versus 1/α of sample p-a recorded at 94 Hz for SPV=0.3 mV.*

SAMPLE	94 Hz	471 Hz
p-sub	213 ± 14	200 ± 16
p-a	71 ± 5	86 ± 5
p-b	158 ± 15	149 ± 13
p-c	159 ± 11	153 ± 9

***Table 4.1.1.** Electron diffusion length (in μm) found in the samples under study.*

The as-grown sample (p-a) shows strongly reduced *L* values as compared to the other samples. This supports the above consideration of large recombination velocity via SS related to structural defects formed during the MACE process. Samples p-b and p-c have similar *L* values, which means that their τ_{eff} are similar in agreement with the similar SPV phase values

measured in these samples (see Sect. 4.1.2). In addition, this suggests that already the first chemical treatment (p-b) results in the lift-off of the tiny Si nanostructures at the SiNW surface, thus resulting in smoother surface, reduced SS density and a substantial increase in the L value.

The values of *L* obtained at 94 and 471 Hz are very close to each other for samples p-sub, p-b and p-c, which corresponds to the expectations considering the relatively low frequencies used. However, contrary to what happens in the chemically treated samples, in the as-grown sample p-a *L* is higher at 471 Hz as compared to 94 Hz. This suggests the existence in this sample of relatively slow traps, whose impact on the electron transport decreases with increasing frequency. The concentration of these traps decreases substantially in the chemically treated samples p-b and p-c leading to higher *L* values. This finding is in agreement with the intriguing slow SPV process observed in the LES of the SPV spectra, which is strongly reduced by the chemical treatment (see above). The origin of these slow traps may be related to the rough SiNW surface of the as-grown sample.

4.1.4. Conclusions

A large concentration of positively charged surface recombination centres is present in the MACE as-grown samples, which decrease the carrier lifetime and diffusion length and increase the surface band bending. Their concentration is strongly reduced after the chemical treatment with HF/piranha/HF, which lifts off the tiny Si nanostructures at the Si NW surface and improves the quality of the SiNWs.

4.2. GaAs-based diluted nitrides materials

There has been great interest in dilute nitride III-V-N materials during the last two decades, driven in part by their potential application in multijunction solar cells (MJSC). The performance of MJSCs solar cells is limited by the performance of the subcells which need to be chosen for their bandgaps and also need to be grown with appropriate crystal quality. Dilute nitride alloys such as InGaAs(Sb)N and GaAsSbN can provide adjustable bandgaps between 0.7 and 1.2 eV while remaining lattice-matched to GaAs or Ge substrates. Hence the development of these materials is of great significance for high-efficiency multijunction solar cells, where they can be used to collect low-energy photons. However, the device's performance has not reached expectations due to low minority carrier diffusion lengths. Therefore, further investigations are needed to improve the properties of dilute nitrides.

At the time when these studies were undertaken, there were no reports on LPE-grown InGaAsSbN and GaAsSbN. Therefore, the data for the structural, optical and electronic properties of these materials were scarce and they needed to be extensively studied as an alternative to materials fabricated by more conventional techniques like MBE and MOCVD. Besides, SPS was rarely used [34–37] to study dilute nitrides despite the opportunities it offers.

In this section, we present our SPS studies of the electronic and optical properties of dilute nitride layers and solar cell structures grown by liquid phase epitaxy (LPE) described in papers **F11-F15** and **R3-R6**. SPV spectra are recorded at room temperature using the set-up and measurement procedure described in Sect. 2.1. The interpretation of the results is complemented by the information obtained from PL spectra and electronic structure calculations performed by colleagues from different universities (as noted below).

4.2.1. Details of the LPE growth

The LPE growth was carried out in the Central Laboratory of Applied Physics, Bulgarian Academy of Sciences in Plovdiv by M. Milanova. Although it is not a contribution of the author, this information is included in the thesis to show the problems that LPE faces in growing thick dilute nitride layers and this way to better understand the value of the research work presented in the next sections. Since the higher growth temperatures limit the N incorporation because of micro-phase segregation, a low-temperature ($T < 600$ °C) version of

the LPE method was used. To grow single crystalline layers without phase separation the composition of the melt was carefully chosen to be near the boundary of the large miscibility gap of the ternary or quaternary compounds. The samples were grown on (100) n-type GaAs:Si (~10^{18}cm^{-3}) substrates. The starting materials for the solutions consisted of 6N pure solvent metals Ga, In and/or Sb. Polycrystalline GaAs and GaN with a purity of 5N were used as sources of As and N. The nitrogen content in the melt was 0.5 at%.

4.2.2. GaAsN and InGaAsN thick layers. The effect of indium

Epitaxial $GaAs_{1-x}N_x$ layers 1-2 μm thick were prepared from Ga-rich solution from different initial epitaxy temperatures varied in the range of 600 – 550°C. Hall-effect measurements revealed n-type doping of the layers of 6-7×10^{17}cm^{-3}. Figure 4.2.1 represents the SPV spectrum of a GaAsN sample compared with that of the n-GaAs substrate. A red shift of the absorption edge is observed for GaAsN relative to GaAs. To assess the bandgap of the material E_g we plot the square of the SPV vs photon energy, consider the linear part of the obtained curve and extrapolate the straight line to find its intersection with the abscissa. For the current sample, E_g = 1.390 eV and therefore the bandgap shift ΔE_g relative to GaAs (E_g=1.423 eV) is 33 meV. Electronic structure calculations of the bandgap using the semi-empirical tight-binding method[7] [38] have shown that a similar red shift (31 meV) is obtained for N content x = 0.001. This way the N content in the sample is assessed. This result is confirmed by calculations of the imaginary part of the dielectric function of $GaAs_{1-x}N_x$ for x ranging from 0 to 0.01 with a step of 0.001. The comparison with the SPV

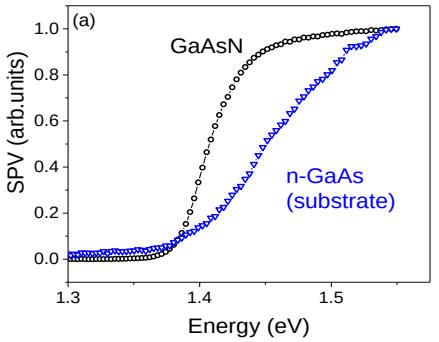

Figure 4.2.1. *Normalized SPV amplitude spectra of the n-GaAs substrate (triangles) and a GaAsN sample (circles).*

[7] The calculations were performed by N. Shtinkov in Ottawa University, Canada.

spectrum from Fig. 4.2.1. has shown that the nitrogen content in the experimental sample is indeed $x = 0.001$ (0.1%) [39].

The low N incorporation efficiency in the layers at near-equilibrium conditions (provided by LPE) is due to the small solubility of N in the Ga-melt and the low N diffusion coefficient into the As-sublattice of GaAsN. It can be increased by introducing several percent of In atoms in the crystal lattice. Under near-equilibrium lattice-matched LPE growth conditions, the nitrogen incorporation efficiency increases to compensate for the compressive strain caused by the large In atoms. Therefore, quaternary layers $In_yGa_{1-y}As_{1-x}N_x$ were fabricated from mixed In + Ga melt. The In content in the layers assessed by EDX[8] is in the range of 1% - 2% ($y \cong 0.01 - 0.02$) depending on the melt composition and epitaxy temperatures.

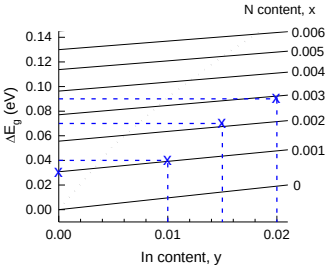

Figure 4.2.2. *Calculated bandgap shifts relative to pure GaAs as a function of the In content (y) in $In_yGa_{1-y}As_{1-x}N_x$ for several N content values (x). The dotted line corresponds to the lattice-matched condition y = 3x. The dashed lines mark the experimentally obtained bandgap shifts and the corresponding In contents.*

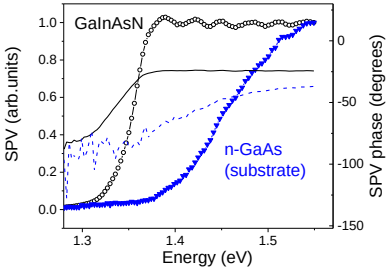

Figure 4.2.3. *SPV amplitude (symbols) and phase (lines) spectra of the n-GaAs substrate (triangles and dashed line) and an InGaAsN sample (circles and solid line).*

Figure 4.2.2 shows the calculated bandgap shifts as a function of the In content in $In_yGa_{1-y}As_{1-x}N_x$ for several values of the N content. For $y = 0$ (i.e.

[8] The EDX and SEM measurements were performed in the Laboratory "Technology of materials" at the Faculty of Physics, Sofia University by S. Russev, K. Genkov and A. Tsonev.

GaAsN) and $x = 0.001$ the red bandgap shift is $\Delta E_g = 31$ meV in agreement with the above experimental finding. Figure 4.2.3 presents the SPV amplitude spectrum of an InGaAsN sample with In content $y \cong 0.015$ (~ 1.5 %) compared with that of the GaAs substrate. The obtained bandgaps are $E_g = 1.350$ eV and $E_g = 1.423$ eV for InGaAsN and GaAs, respectively, which gives $\Delta E_g = 73$ meV. Comparing the values of y and ΔE_g with the curves from Fig. 4.2.2 we obtain $x \cong 0.002$ (~0.2%) for the N content in this sample. Similar considerations applied to samples with In content ~ 2% give $\Delta E_g \cong 90$ meV and therefore $x \cong 0.003$ (0.3%). In samples with ~1% In content $\Delta E_g \cong 40$ meV and therefore $x \cong 0.001$ (0.1%). The above-described results confirm that the N content in the layers increases with increasing the In content.

The bandgap red shifts of the investigated InGaAsN samples are quite larger as compared to the calculated red shifts of InGaAs due to In. Therefore, they are mainly due to the presence of N in the samples.

To check whether the bandgap red shift is temperature-dependent, PL measurements[9] at room temperature and 2 K are carried out on some InGaAsN samples. It has been found that the bandgap determined from the PL peak position at 2 K and 300 K is red-shifted by the same value relative to the GaAs bandgap at the corresponding temperature.

Figure 4.2.3. also shows that the SPV phase spectra of the InGaAsN and GaAs samples are in the IVth quadrant, which confirms the n-type doping found by Hall-effect measurements. The phase spectra suggest also that the energy band bending at the interface layer/substrate is also upwards. This is expected from the lower doping of the layer as compared to the substrate.

4.2.3. InGaAsN and InGaAsSbN thick layers. The effect of antimony

Nearly lattice-matched to GaAs quaternary $In_yGa_{1-y}As_{1-x}N_x$ layers were grown from In-rich melt (90%In +10%Ga) containing 0.5 at.% polycrystalline GaN as a nitrogen source. The crystallization was carried out from different initial epitaxy temperatures in the range 580 – 560 ºC. To study the effect of small quantity Sb incorporation in the lattice of InGaAsN keeping the structure

[9] PL spectra of dilute nitride layers were recorded at 300 K by I. Asenova at Imperial College of London and K. Kirilov at Sofia University. I. G. Ivanov measured PL spectra at 2 K at Linköping University.

quasi-lattice matched to GaAs a series of epitaxial $In_yGa_{1-y}As_{1-x-z}Sb_zN_x$ layers was prepared. They were grown from a mixed 86%In + 10%Ga + 4%Sb growth solution applying the same temperature regimes as for the quaternary InGaAsN compounds. The thickness of the layers determined by SEM is in the range of 2–2.5 μm depending on the initial epitaxy temperature and growth time. EDX measurements revealed ~3% In content ($y \cong 0.03$) in the samples. The N content estimated from high-resolution XRD curves[10] using Vegard's law [40] is about 0.27% ($x \cong 0.0027$). A bit larger lattice mismatch to the GaAs substrate is found for the InGaAsSbN layers (0.20% vs 0.16% in InGaAsN). This agrees with the incorporation in the lattice of ~0.5% Sb ($z \cong 0.005$), as determined by EDX.

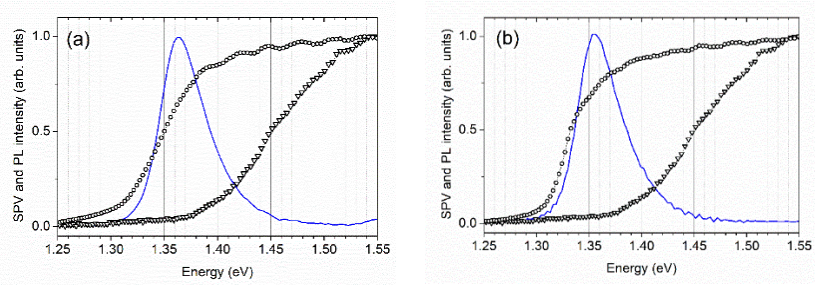

Figure 4.2.4. *Normalized SPV (circles) and PL (line) spectra of (a) InGaAsN and (b) InGaAsSbN. The SPV spectra of the GaAs substrate are represented by triangles.*

The SPV amplitude spectra of InGaAsN and InGaAsSbN samples are compared with the SPV spectrum of the GaAs substrate in Fig. 4.2.4 (a) and (b), respectively. In both cases, a red shift of the absorption edge is observed relative to GaAs. For the InGaAsN sample, E_g = 1.328 eV and therefore the red shift is 95 meV. For the InGaAsSbN sample, E_g = 1.312 eV and the red shift is 111 meV. The PL spectra in Fig. 4.2.4 reveal relatively broad peaks interpreted as band-edge luminescence. The exponential tail at the high-energy side of the

[10] XRD measurements were performed by J.W. Gerlach (Leibniz Institute for Surface Modification) and G. Avdeev (Inst. of Physical Chemistry, Bulgarian Academy of Sciences).

peak results from the Boltzmann carrier distribution, while that at the low-energy side is attributed to localised states within the bandgap. Both SPV and PL spectra of InGaAsSbN are shifted to lower energies relative to the spectra of InGaAsN.

The above-described comparisons between SPV and PL are performed for several InGaAsN and InGaAsSbN samples. In all cases, a decrease in the bandgap of the dilute nitrides relative to GaAs is observed. The addition of Sb further reduces the bandgap, which is in agreement with literature data for GaAsSbN [41] and GaAsSb [42] and semi-empirical tight-binding calculations results for InGaAsSbN [43]. This is due to the increase of the valence band maximum with increasing Sb content. However, the bandgap shift relative to GaAs observed in the InGaAsSbN samples is mostly due to the effect of N since the coupling between the N level and the CB minimum of the host material is stronger than the effects of Sb and In.

As a general tendency, the bandgap values found by SPS in our samples are lower by some 30-45 meV than those obtained by PL. We have proposed an explanation of this "anti-Stokes shift" [43]. It includes N-induced defect states in the bandgap below the CB edge, thermal emission of carriers from these localized states and dominance of band-to-band recombination observed in the PL experiment. The existence of a tail of defect states below the CB is evidenced by the low-energy tail of the PL spectra in Fig. 4.2.4 as well as of the PL spectrum measured at 2K [39]. On the other hand, in the SPS measurements with increasing the photon energy, the defect states in the bandgap near the CB are reached first and the electrons thermally escape to the continuum. Thus, SPS gives a bit lower energy for the optical absorption edge as compared to PL. Another reason for the lower bandgap values found by SPS could be related to Franz-Keldysh effect arising due to the electric field in the SCR at the layer surface and interface. A similar "anti-Stokes shift" between the optical absorption and PL spectra was observed also in [44] in GaAsN layers with low N content ($x = 0.006$).

To determine the dominant recombination mechanisms in our InGaAsSbN layers the integrated PL intensity I_{PL} has been studied as a function of the excitation power I_{exc}. The dependence $I_{PL}(I_{exc})$ in various semiconductors is usually represented as a power function $I_{PL} \sim I_{exc}^{k}$ [45], however, we could not find such studies concerning dilute nitride alloys. Following the model from [45]

and considering that in our case the excess concentration of electrons is much less than the equilibrium one, we expect $k = 1$ in the dependence $I_{PL} \sim I_{exc}^{k}$. The values obtained in different samples vary between 1.0 and 1.2. Thus, we conclude that the dominant radiative recombination mechanisms are free carrier recombination and exciton recombination.

4.2.4. GaAsSbN layers and solar cell structures

4.2.4.1. Single GaAsSbN layers

The crystallization of monocrystalline $GaAs_{1-x-y}Sb_yN_x$ layers without phase separation was carried out from a mixed 95 at.% Ga + 5 at. % Sb solution performed from different initial epitaxy temperatures in the range 575 – 555°C. The Sb content of ~6.8% ($y \cong 0.068$) in the GaAsSbN layers was determined by EDX and confirmed by XPS[11]. The N composition evaluated from XPS and XRD applying Vegard's law is ~ 0.1% ($x = 0.001$). The layer thickness found by SEM on the cross-section of different samples is in the range of 0.5–1.2 μm.

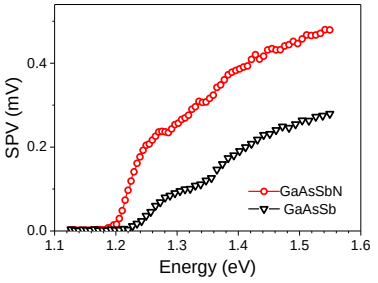

Figure 4.2.5. *SPV amplitude spectra of GaAsSbN (circles) and GaAsSb (triangles) layers.*

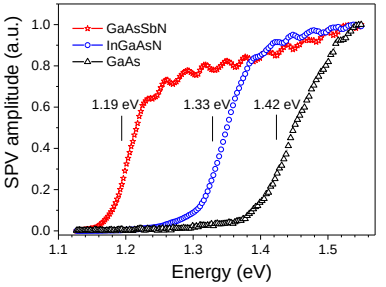

Figure 4.2.6. *Normalized SPV spectra of GaAsSbN and InGaAsN layers compared to that of GaAs substrate.*

Figure 4.2.5 displays the SPV amplitude spectra of a GaAsSbN and a GaAsSb single-layer samples with the same amount of Sb ($y \cong 0.068$) grown under identical growth conditions. The spectrum of GaAsSbN shows a larger signal by a factor, which increases from 1.8 at 800 nm (1.55 eV) to 8.0 at 1000

[11] The XPS measurements were performed by K. Kostov (Institute of General and Inorganic Chemistry, Bulgarian Academy of Sciences).

nm (1.24 eV) indicating better photo-response. Therefore, adding nitrogen into GaAsSb even at ultra-dilute level improves the photo-response of the material. The improvement is more pronounced for photon energies below the GaAs bandgap. This could be explained as follows. The strain effects caused by Sb and N atoms are opposite in sign: Sb tries to expand, while N tries to shrink the crystal lattice. Therefore, N in small quantities partially passivates the Sb-related localized states in the bandgap of GaAsSb and this way weakens the carrier trapping effects in the alloy.

In addition, the spectrum of the GaAsSbN sample reveals a clear red shift of the optical absorption edge relative to the GaAsSb sample. The bandgap assessed from the Tauc plot is 1.212 eV and 1.241 eV for GaAsSbN and GaAsSb, respectively. The red shift is therefore 29 meV. If the band anti-crossing model [46] is applied, this value corresponds to a nitrogen content $x \approx 0.001$ in agreement with the XPS and XRD results and the expectations about the role of nitrogen in reducing the bandgap (see Sect. 4.2.2.) The red shift of the GaAsSbN bandgap relative to GaAs is 211 meV. This is nearly twice larger as compared to the red shift found in the In-containing samples discussed above. It is mainly due to the larger Sb content (~7 %) in this material, which moves the VB edge toward higher energies this way further decreasing the bandgap. To illustrate this difference Figure 4.2.6 presents SPV spectra of a GaAsSbN and an InGaAsN samples compared to that of the GaAs substrate. The bandgap of GaAsSbN assessed from the Tauc plot is 140 meV lower as compared to InGaAsN. Its red shift relative to GaAs is 233 meV, which is the larger value obtained in our experiments.

4.2.4.2. GaAsSbN based solar cell structures

In addition to single GaAsSbN epitaxial layers, a series of p-i-n structures (Fig. 4.2.7.) ***p-AlGaAs – p-GaAs – i-GaAsSbN – n-GaAs*** were grown based on GaAsSbN layers compensated by Mg doping, which electron concentration is as low as 8.7×10^{14}cm^{-3} as found by Hall-effect measurements. Figure 4.2.7 presents the SPV amplitude and phase spectra of such a p-i-n structure. The amplitude reveals a step in the range of 1.24 – 1.38 eV originating from the absorption in GaAsSbN and another step for $h\nu > 1.38$ eV due to the GaAs layers. The signals from GaAsSbN and GaAs are comparable in magnitude, which indicates the good quality of the dilute nitride layer.

The absorption edge of GaAsSbN found by the Tauc plot in different p-i-n samples varies in the range of 1.200 eV – 1.262 eV. Considering its thickness and Hall carrier concentration the GaAsSbN layer is fully depleted and the

photogenerated electrons are swept towards the *n*-GaAs layer, while the holes – toward the p^+-GaAs layer and thus give rise to photovoltage. The direction of the carrier drift is evidenced by the SPV phase values, which are close to zero degrees in agreement with the upward energy bands bending (in the direction towards the surface) in the p-i-n structure.

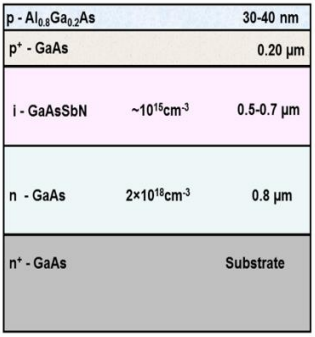

Figure 4.2.7. *Schematic of the layer sequence in the p-i-n structure*

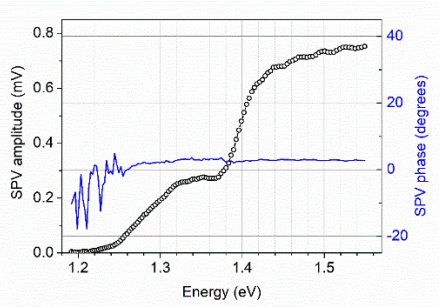

Figure 4.2.8. *SPV amplitude (symbols) and phase (line) spectra of a p-i-n solar cell based on compensated GaAsSbN.*

PL measurements of the p-i-n structures are performed at different temperatures using high[12] (140mW) and low[13] (0.55mW) laser excitation power. The PL spectra taken at high excitation (not shown here) at temperatures from 20 K to 300 K are dominated by a large peak due to the radiative recombination in GaAsSbN, which is the material with the lowest bandgap in the structure. The integrated PL intensity of this peak is studied as a function of the temperature using the Arrhenius plot. The activation energy of 57 meV is found similar to the value we have obtained in single GaAsSbN layers (49 meV [47]). It is explained by the activation of non-radiative recombination channels with increasing temperature, which are related to N-induced defects in the crystal lattice.

[12] PL spectra with high excitation were recorded by D. Alonso-Álvarez at Imperial College London

[13] PL spectra with low excitation were measured by G. M. Piana at the University of Southampton

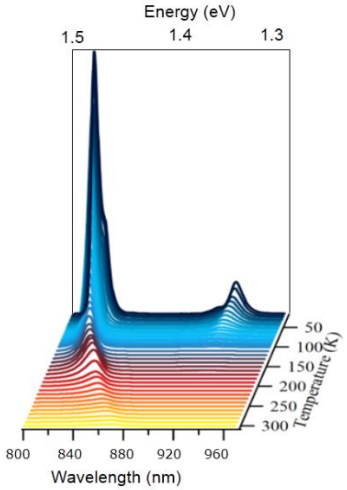

Figure 4.2.9*. PL spectra of a p-i-n structure measured at low excitation (0.55 mW) at different temperatures in the range 11–300K.*

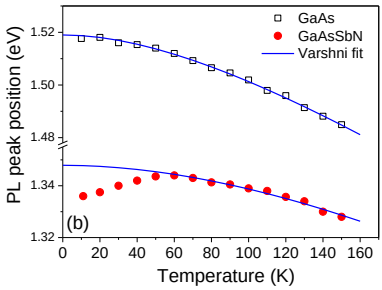

Figure 4.2.10*. Temperature dependence of the PL peak energy of GaAsSbN (red circles) and GaAs (black squares) in the p-i-n structure from Fig. 4.2.9. The lines represent Varshni's fits of the data.*

The PL spectra measured with low excitation in the range 11 K – 300 K are depicted in Fig. 4.2.9 . The peak with high intensity comes from the p+ GaAs layer, while the peak from the GaAsSbN layer in the structure is weaker and red-shifted. The variations of the GaAsSbN PL peak energy as a function of the temperature are shown in Fig. 4.2.10. The peak exhibits a non-typical S-curve (blue shift – red shift) behaviour. The first red shift is missing, while the blue shift is only around 10 meV. This indicates that the potential fluctuations in the GaAsSbN layer are relatively small and even at low temperatures the excitons receive enough thermal energy to escape from the localized states and transfer to higher-energy states in the band-tail closer to the conduction band. In another sample of a single GaAsSbN layer, we have obtained a blue shift of 27 meV [48] attesting to deeper potential fluctuations. Blue shifts of the same order of

magnitude as in our samples were reported for MBE-grown GaAsSbN/GaAs single quantum wells with larger N content, however after annealing [49,50].

In the case of high excitation, no blue shift has been observed (not shown here). This is explained by the filling of the localized states in the bandgap and the domination of band-to-band emission. As stated by other authors [50], the excitation level should be taken into account when analysing the temperature dependence of the PL peak energy to assess the carrier localization energy.

A few of the fabricated p-i-n structures were used for measurements of I-V curves and external quantum efficiency (EQE)[14]. Photovoltaic parameters are measured on several devices. The best solar cell shows an efficiency of 4.15 %. It is comparable to the efficiency reported for single-junction 1.25 eV GaAsSbN solar cells grown by MOCVD [51]. Higher efficiency of about 6 % has been achieved for 1.15 eV MBE grown GaAsSbN solar cells [52]. In both cases, rapid thermal annealing at 800°C of the solar cells was performed, which significantly increased the open-circuit voltage values to 0.5 – 0.6 V due to the decrease of the density of the localized states. Typical values of V_{oc} measured in our solar cells based on as-grown LPE structures without rapid thermal annealing are in the range of 0.40 − 0.44 V, while the efficiency varies in the range of 4.00 − 4.15%.

EQE values of around 50 % are observed in the wavelength range 550 – 850 nm, which suggests that the upper p^+-GaAs emitter layer is of good quality despite being grown on GaAsSbN. A significant decrease of the EQE in the infrared part of the spectrum is due to the short minority carrier diffusion length in the dilute nitride layer because of the efficient recombination via localized defect levels. Nevertheless, the EQE extends to approximately 1040 nm (1.19 eV) with an inflexion point at 1.26 eV in agreement with the SPV results for the GaAsSbN bandgap.

4.2.5. Conclusions

SPS combined with PL has been used to study GaAs-based dilute nitrides materials prepared by LPE. Layers with good photoresponse have been obtained nearly lattice-matched to GaAs. Adding In increases the incorporation of N in

[14] The I-V and EQE measurements were performed by A. Muntaz at the University of Liverpool.

the crystal lattice of InGaAsN layers and further decreases the bandgap. The dominant radiative recombination mechanisms in the InGaAs(Sb)N layers are free carrier and exciton recombination. Bandgap values as low as 1.2 eV have been measured in GaAsSbN layers. The potential fluctuations are of the order of 10–30 meV similar to other reported values. p-i-n solar cell structures based on GaAsSbN layers compensated by Mg doping have shown power conversion efficiencies above 4 % and open-circuit voltages above 0.4 V even without anti-reflection coatings and rapid thermal annealing. The obtained results reveal the capacity of the LPE method for growing dilute nitrides layers and structures as promising materials for photovoltaic applications.

MAIN RESULTS and CONTRIBUTIONS

The contributions in the thesis are in three directions - i) design, construction and improvement of the SPS setup; ii) development of novel approaches for retrieving information from the SPV spectra; and iii) the application of the developed setup and methodology in the study of various materials and nanostructures for optoelectronics and photovoltaics. The results of the latter direction on the one hand demonstrate the practical application of the developed SPS setup and novel approaches, and on the other hand, have an independent significance in each specific case by providing new information and knowledge on the investigated structures and phenomena. The contributions are summarized below.

1. An experimental setup and measurement procedure for SPS in the MIS operation mode have been developed, allowing SPV measurements in a wide spectral and temperature range.

2. For the first time, the zero value of the SPV phase has been defined. On this basis, two novel approaches have been developed for retrieving information from the SPV phase spectra and implemented for the characterization of bulk semiconductors and nanostructures, as follows.

a) It is shown that the SPV phase is in the IV^{th} quadrant for upward and in the II^{nd} quadrant for downward energy band bending at the location in the sample, where the SPV signal is generated (surface or buried interface). In particular, this can be a handy tool for determining the semiconductor type (n or p).
b) The decrease of the SPV phase delay with increasing the free carrier generation rate has been qualitatively explained by proposing three mechanisms that decrease the excess carrier lifetime and lead to non-linear recombination. In such cases, the SPV phase spectrum reflects the features of the optical absorption coefficient spectrum similarly to the amplitude spectrum.

The need for a combined analysis of the SPV amplitude and phase spectral behaviour to correctly interpret the SPV experimental data is demonstrated. To facilitate this analysis a vector model for the SPV signal is developed. The model is especially useful when more than one SPV generation

process occurs in the same spectral range leading to complicated and intriguing SPV spectral features.

3. A pioneering SPS study of **short-period AlAs/GaAs superlattices (SLs) containing GaAs embedded quantum wells (EQWs)** with graded interfaces has been performed, as follows.

a) The exciton transition energies in the EQWs and the SLs have been determined from the SPV spectra and a very good agreement is found with the values obtained by PL data and envelope function approximation calculations. The degree of interface grading has been assessed from the comparison between calculated and experimental values. It is smaller in samples gown at lower temperature and with a buffer layer between the substrate and the first SL.

b) It is demonstrated that the SPV spectral shape of the nanostructures and its excitation density dependence can be significantly affected by the substrate type.

c) The contribution of free excitons has been found to dominate the radiative recombination from low up to room temperature.

4. The first SPS studies have been conducted on three types of multilayer structures with quantum dots, prospective for applications in light emitters, IR photodetectors and optical memories, respectively. The combined analysis of the amplitude and phase SPV spectra and the comparison with the PL results have allowed us to identify the interband optical transitions in the quantum dots and determine their energies.

- In the **InAs/InGaAlAs/InP** quantum dash-in-well structures the blue shift of the inter-band optical transition energies resulting from the controlled interface intermixing has been registered by SPS and confirmed by PL.
- The optical transition energies are highest in the sub-monolayer **InAs/GaAs** QDs due to their small size.
- The optical transition energies in the **InP/GaAs** QDs, are lower than those in isolated QDs of the same type due to the interaction of QDs from adjacent planes and their coupling into quantum pillars.

• Using the vector model, the contribution of the substrate, which leads to non-trivial SPV spectral structures, is clarified.

5. An original SPS study has been performed on **Si nanowires** prepared by metal-assisted chemical etching (MACE) designed for light trapping in c-Si solar cells. It is shown that the chemical treatment with HF/piranha/HF strongly reduces the surface recombination centres produced by the etching process and this way increases the minority carrier diffusion length twice.

6. Extensive SPS and PL studies have been performed on **GaAs-based dilute nitride** layers and solar cell structures grown by **liquid phase epitaxy** (LPE). The investigations have a pioneering character in most of the cases and partially fill the gap of information concerning the properties of LPE-grown GaAs-based dilute nitrides.

a) It is shown that adding In increases the incorporation of N in the crystal lattice, this way further reducing the bandgap.

b) The absorption edge of GaAsN, InGaAsN, and InGaAsSbN has been determined. Its red shift relative to GaAs is mainly due to the effect of N on the conduction band edge. Bandgap values as low as 1.2 eV have been measured in GaAsSbN layers and explained by the effect of the Sb on the valence band edge.

c) The intriguing “anti-Stokes” shift between absorption (SPS) and emission (PL) of the InGaAs(Sb)N layers has been explained by absorption via N-induced defect states near the conduction band edge.

d) It is shown that the dominant radiative recombination mechanisms in InGaAs(Sb)N are free carrier recombination and exciton recombination.

e) The potential fluctuations in the GaAsSbN layers leading to carrier localization at low temperatures have been assessed to be of the order of 10-30 meV similar to the values reported for annealed GaAsSbN/GaAs QWs.

f) SPS has been used to determine the low-energy optical absorption edge of the first LPE-grown solar cells based on GaAsSbN

compensated by Mg doping. A very good agreement is found with the spectrum of the external quantum efficiency.

In a **fundamental** aspect, the research presented in the thesis contributes to the systematic and in-depth study of the optical and electronic properties of advanced semiconductor optoelectronic materials and nanostructures. At the same time, addressing some less-studied problems of the SPV technique helps to improve the **analysis** of experimental data and to expand the applications of SPV spectroscopy. In the **applied** aspect, the obtained results are of interest for the creation of new optoelectronic, photonic and photovoltaic discrete components and integrated circuits. In addition, they demonstrate the potential of the SPS as a viable highly sensitive tool for advanced characterization of various semiconductor materials and complex nanostructures at room temperature.

LIST OF PUBLICATIONS INCLUDED IN THE THESIS

Publications in scientific journals with IF

F1. **V. Donchev**, N. Shtinkov, K. Germanova, I. Ivanov, H. Brachkov, Tzv. Ivanov
"Photoluminescence Line-Shape Analysis in Quantum Wells Embedded in Superlattices"
Mat. Sci. Eng., C **15**, (1-2) 75-77 (2001). **IF=0.905**

F2. **V. Donchev**, K. Kirilov, Ts. Ivanov, K. Germanova
"Surface photovoltage phase spectroscopy– a handy tool for characterisation of bulk semiconductors and nanostructures"
Mater. Sci. Eng., B **129** (1-3) 186-192 (2006). **IF=1.331**

F3. Ts. Ivanov, V**. Donchev**, Y. Wang, H. S. Djie, and B. S. Ooi
"Interdiffused InAs/InGaAlAs quantum dashes-in-well structures studied by surface photovoltage spectroscopy"
J. Appl. Phys. **101** (11) 114309 (2007) **IF=2.171**

F4. Ts. Ivanov, **V. Donchev**, K. Kirilov, K. Germanova
"Surface photovoltage investigation of GaAs quantum wells "
J. Optoel. & Adv. Mat. **9** (1) 190-193 (2007). **IF=0.827**

F5. **V. Donchev**, K. Kirilov, Ts. Ivanov, K. Germanova
"A surface photovoltage spectroscopy study of GaAs/AlAs complicated nanostructures with graded interfaces"
J. Appl. Phys. **101** (10) 124305 (2007). **IF=2.171**

F6. Ts. Ivanov, **V. Donchev**, K. Germanova and K. Kirilov
"A vector model for analyzing the surface photovoltage amplitude and phase spectra applied to complicated nanostructures"
J. Phys. D: Appl. Phys. **42** (13) 135302 (2009). **IF=2.083**

F7. Ts. Ivanov, **V. Donchev,** K. Germanova, P. F. Gomes, F. Iikawa, M. J. S. P. Brasil and M. A. Cotta
"Optical properties of multi-layer type II InP/GaAs quantum dots studied by surface photovoltage spectroscopy"
J. Appl. Phys. **110** , 064302 (2011). **IF=2.168**

F8. F. Iikawa, **V. Donchev**, Ts. Ivanov, G. O. Dias, L. H. G. Tizei, R. Lang, E. Heredia, P. F. Gomes, M. J. S. P. Brasil, M. A. Cotta, D. Ugarte, J. P. Martinez Pastor, M. M. de Lima Jr., and A. Cantarero
"Spatial carrier distribution in InP/GaAs type II quantum dots and quantum posts"
Nanotechnology **22**, 065703 (2011). **IF=3.979**

F9. **V. Donchev**, Ts. Ivanov, Ts. Ivanova, S. Mathews, J. O. Kim and S. Krishna
"Surface photovoltage spectroscopy study of InAs quantum dot in quantum well multilayer structures for infrared photodetectors"
Superlattices and Microstr. **88,** 711–722 (2015). **IF=** 2.117

F10. **V. Donchev**, S. Georgiev, I. Leontis and A. G. Nassiopoulou
"Effective Removal of Surface Recombination Centers in Silicon Nanowires Fabricated by Metal-Assisted Chemical Etching"
ACS Appl. Energy Mater. **1** (8) 3693–3701 (2018). **IF=4.473**

F11. **V. Donchev** , M. Milanova, I. Asenova, N. Shtinkov, D. Alonso-Álvarez, A. Mellor, Y. Karmakov, S. Georgiev and N. Ekins-Daukes
"Effect of Sb in thick InGaAsSbN layers grown by liquid phase epitaxy"
J. Cryst. Growth **483 1**40–146 (2018). **IF=1.573**

F12. M. Milanova, **V. Donchev**, K. L. Kostov, D. Alonso-Álvarez, P. Terziyska, G. Avdeev, E. Valcheva, K. Kirilov and S. Georgiev
"Study of GaAsSb:N bulk layers grown by liquid phase epitaxy for solar cells applications"
Mat. Res. Express **6** (7) 075521 (2019). **IF=1.929**

F13. **V. Donchev**
"Surface photovoltage spectroscopy of semiconductor materials for optoelectronic applications" (Tutorial)
Mater. Res. Express **6** 103001 (2019), **IF=1.929**

F14. M. Milanova, **V. Donchev**, B. Arnaudov, D. Alonso-Álvarez, P. Terziyska
"GaAsSbN-based p-i-n heterostructures for solar cell applications grown by liquid-phase epitaxy"
J. Mater. Sci.: Mater. Electron. **31** (3), 2073–2080 (2020). **IF=2.478**

F15. M. Milanova, V. Donchev, K. J. Cheetham, Zh. Cao, I. Sandall, G. M. Piana, O. S. Hutter, K. Durose, A. Mumtaz
"Single-junction solar cells based on p-i-n GaAsSbN heterostructures grown by liquid phase epitaxy"
Solar Energy **208**, 659-664 (2020). **IF=5.742**

Conference papers in scientific journals with impact rang

R1. **V. Donchev**, Ts. Ivanov, Y. Wang, H. S. Djie, B. S. Ooi
"Surface photovoltage spectroscopy of interdiffused InAs/InGaAlAs quantum dashes-in-well structure"
phys. stat. sol. (c) **4 (**2) 412– 414 (2007)
(poster at Int. Conf. on Superlattices, Nanostructures and Nanodevices, 30.07- 04.08., 2006, Istanbul, Turkey)

R2. Ts. Ivanov, **V. Donchev**, K. Bachev, Y-H. Ding, Y. Wang, H. S. Djie and B. S. Ooi
"Bandgap engineering of InAs/InGaAlAs quantum dashes-in-well laser structures : A surface photovoltage spectroscopy study"
J. Phys. Conf. Ser. **113,** 012033 (2008)
(poster presented at VEIT-2007, September, 2007, Varna, Bulgaria)

R3. **V. Donchev**, M. Milanova, J. Lemieux, N. Shtinkov and I. G. Ivanov
"Surface photovoltage and photoluminescence study of thick Ga(In)AsN layers grown by liquid-phase epitaxy"
J. Phys. Conf. Ser. **700** (1) 012028 (2016)
(poster at 19th International Summer School on Vacuum, Electron and Ion Technologies, 21 − 25 September 2015, Sozopol, Bulgaria)

R4. **V. Donchev**, I. Asenova, M. Milanova, D. Alonso-Álvarez, K. Kirilov, N. Shtinkov, I. G. Ivanov, S. Georgiev, E. Valcheva and N. Ekins-Daukes
„Optical properties of thick GaInAs(Sb)N layers grown by liquid-phase epitaxy"
J. Phys. Conf. Ser. **794,** 012013 (2017)
(poster at the 19th ISCMP-2016, 29.08 – 02.09.2016, Varna, Bulgaria)

R5. **V. Donchev**, M. Milanova, S. Georgiev, K. L. Kostov and K. Kirilov
"Dilute nitride InGaAsN and GaAsSbN layers grown by liquid-phase epitaxy for photovoltaic applications"
J. Phys. Conf. Series **1492,** 012049 (2020)
(poster at the 21th International Summer School on Vacuum, Electron and Ion Technologies, 23 − 27 September 2019, Sozopol, Bulgaria)

R6. **V. Donchev**, M.Milanova.
"Dilute nitrides heterostructures grown by liquid phase epitaxy for solar cells applications"
J. Phys. Conf. Series **1762,** 012025 (2021)
(invited lecture at the 21th International School on Condensed Matter Physics, 31.08 – 04.09.2020, Varna, Bulgaria)

Publications in other scientific journals

O1. **V. Donchev**, Ts. Ivanov, K. Germanova, K. Kirilov
"Surface photovoltage spectroscopy – an advanced method for characterization of semiconductor nanostructures" (Review)
Trends in Applied spectroscopy **8,** 27- 66 (2010)

O2. S. Georgiev, **V. Donchev**, M. Milanova
"Surface Photovoltage Spectroscopy Characterization of GaAsSbN Layers Grown by Liquid-Phase Epitaxy"
Chemistry. Bulgarian Journal of Science Education, **27**, 658-665 (2018)
(poster at the National Forum in Physics "Physics Forever Young Science", 27.- 29. October, 2017, Varna, Bulgaria)

O3. Tsanimir Angelov , **Vesselin Donchev**, Stefan Georgiev and Kiril Kirilov
"Carrier Lifetime and Phase Retardation of the Photoresponse of Photovoltaic Materials"
J. Phys. and Technol. **2** (1) 3-7 (2018)
(poster at the 6th National Student Scientific Conference on Physics and Engineering Technologies, 16-18. November, 2017 Plovdiv Bulgaria)

Acknowledgements

I would like to thank my whole family for their patience and help in daily household chores and especially my wife Albena, whose scientific insights have always been a stimulus and support for me. I am grateful to my colleagues K. Germanova, K. Kirilov, Ts. Ivanov and S. Georgiev for the fruitful collaboration in the development of the SPS technique and measurement methodology in our laboratory. I thank M. Milanova for the growth of the dilute nitrides samples and the productive cooperation on this topic in the last 7-8 years. I thank all colleagues from the Department of Condensed Matter Physics and Microelectronics with whom I had the pleasure to work, as well as the colleagues from other departments and universities who contributed in one way or another to the research results presented in the thesis.

References

[1] V. V. Mitin, V.A. Kochelap, M. Dutta, M.A. Stroscio, Introduction to Optical and Optoelectronic Properties of Nanostructures, Cambridge University Press, 2019. https://doi.org/10.1017/9781108674522.

[2] L. Kronik, Y. Shapira, Surface photovoltage phenomena: Theory, experiment, and applications, Surf. Sci. Rep. 37 (1999) 1–206. https://doi.org/10.1016/S0167-5729(99)00002-3.

[3] A. Pan, X. Zhu, Optoelectronic properties of semiconductor nanowires, in: J. Arbiol, Q. Xiong (Eds.), Semicond. Nanowires Mater. Synth. Charact. Appl., Elsevier, 2015: pp. 327–363. https://doi.org/10.1016/B978-1-78242-253-2.00012-8.

[4] V. Donchev, Surface photovoltage spectroscopy of semiconductor materials for optoelectronic applications, Mater. Res. Express. 6 (2019) 103001. https://doi.org/10.1088/2053-1591/ab3bf.

[5] T.K. Sharma, S. Kumar, Surface photovoltage spectroscopy of semi-insulating GaAs in the 800–1100 nm range, Appl. Phys. Lett. 79 (2001) 1715–1717. https://doi.org/10.1063/1.1402657.

[6] J.E. Park, D.K. Schroder, S.E. Tan, B.D. Choi, M. Fletcher, A. Buczkowski, F. Kirscht, Silicon Epitaxial Layer Lifetime Characterization, J. Electrochem. Soc. 148 (2001) G411–G419. https://doi.org/10.1149/1.1380257.

[7] G. Dumitras, H. Riechert, H. Porteanu, F. Koch, Surface photovoltage studies of $In_xGa_{1-x}As$ and $In_x Ga_{1-x}As_{1-y}N_y$ quantum well structures, Phys. Rev. B. 66 (2002) 205324. https://doi.org/10.1103/PhysRevB.66.205324.

[8] В.Л. Бонч-Бруевич, С.Г. Калашников, Физика полупроводников, Наука-ФМ, София, 1977.

[9] J. Wilson, J.F.B. Hawkes, Optoelectronics an introduction, Prentice Hall, London, 1998.

[10] T. Angelov, V. Donchev, S. Georgiev, K. Kirilov, Carrier Lifetime and Phase Retardation of the Photoresponse of Photovoltaic Materials, J. Phys. Technol. 2 (2018) 3–7.

[11] T. Ivanov, V. Donchev, K. Germanova, K. Kirilov, A vector model for analysing the surface photovoltage amplitude and phase spectra applied to complicated nanostructures, J. Phys. D. Appl. Phys. 42 (2009) 135302. https://doi.org/10.1088/0022-3727/42/13/135302.

[12] N. Bachrachashkenasy, L. Kronik, Y. Shapira, Y. Rosenwaks, M.C. Hanna, M. Leibovitch, P. Ram, Surface photovoltage spectroscopy of quantum wells and superlattices, Appl. Phys. Lett. 68 (1996) 879–881.

[13] N. Ashkenasy, M. Leibovitch, Y. Rosenwaks, Y. Shapira, K.W.J. Barnham, J. Nelson, J. Barnes, GaAs/AIGaAs single quantum well p-i-n structures: A surface photovoltage study, J. Appl. Phys. 86 (1999) 6902–6907. https://doi.org/10.1063/1.371770.

[14] V. Donchev, K. Kirilov, T. Ivanov, K. Germanova, A surface photovoltage spectroscopy study of GaAs/AlAs complicated nanostructures with graded interfaces, J. Appl. Phys. 101 (2007) 124305. https://doi.org/10.1063/1.2740357.

[15] V. Donchev, K. Germanova, N. Shtinkov, S.J. Vlaev, Electronic structure and optical properties of AlAs/GaAs superlattices containing embedded GaAs quantum wells, in: Oliver T. Chang (Ed.), Front. Semicond. Res., Nova Science Publishers, Inc., New York, 2006: pp. 25–60.

[16] R.K. Kupka, Y. Chen, Excitonic binding energies in diffused-intermixed GaAs/AlAs/AlGaAs double barrier quantum wells, J. Appl. Phys. 77 (1998) 1990. https://doi.org/10.1063/1.359574.

[17] H. Ruda, a. Shik, Surface photovoltage in quantum well structures, J. Appl. Phys. 91 (2002) 6476–6480. https://doi.org/10.1063/1.1473665.

[18] V. Donchev, K. Germanova, N. Shtinkov, I. Ivanov, S. Vlaev, Photoluminescence study of AlAs/GaAs superlattices containing enlarged wells, Thin Solid Films. 364 (2000) 224–227.

[19] Y. Chen, R. Cingolani, L.C. Andreani, F. Bassani, J. Massies, Photoluminescence in quantum well and bulk GaAs: a direct comparative study, Nuovo Cim. D. 10 (1988) 847–859. https://doi.org/10.1007/BF02450144.

[20] M. Colocci, M. Gurioli, A. Vinattieri, Thermal ionization of excitons in GaAs/AlGaAs quantum well structures, J. Appl. Phys. 68 (1998) 2809. https://doi.org/10.1063/1.346459.

[21] B.S. Ooi, K. McIlvaney, M.W. Street, A.S. Helmy, S.G. Ayling, A.C. Bryce, J.H. Marsh, J.S. Roberts, Selective quantum-well intermixing in GaAs-AlGaAs structures using impurity-free vacancy diffusion, IEEE J. Quantum Electron. 33 (1997) 1784–1792. https://doi.org/10.1109/3.631284.

[22] B.Q. Sun, Z.D. Lu, D.S. Jiang, J.Q. Wu, Z.Y. Xu, Y.Q. Wang, J.N.

Wang, W.K. Ge, Photovoltage and photoreflectance spectroscopy of InAs/GaAs self-organized quantum dots, Appl. Phys. Lett. 73 (1998) 2657–2659. https://doi.org/10.1063/1.122544.

[23] H.S. Djie, B.S. Ooi, V. Aimez, Neutral ion-implantation-induced selective quantum-dot intermixing, Appl. Phys. Lett. 87 (2005) 261102. https://doi.org/10.1063/1.2150279.

[24] H.S. Djie, Y. Wang, D. Negro, B.S. Ooi, Postgrowth band gap trimming of InAs⁄InAlGaAs quantum-dash laser, Appl. Phys. Lett. 90 (2007) 031101. https://doi.org/10.1063/1.2431707.

[25] T.K. Sharma, S. Kumar, K.C. Rustagi, Frequency and intensity dependence of the sub-band-gap features observed in the surface photovoltage spectrum of semi-insulating GaAs, J. Appl. Phys. 92 (2002) 5959–5965. https://doi.org/10.1063/1.1513203.

[26] P.W. Fry, I.E. Itskevich, S.R. Parnell, J.J. Finley, L.R. Wilson, K.L. Schumacher, D.J. Mowbray, M.S. Skolnick, M. Al-Khafaji, A.G. Cullis, M. Hopkinson, J.C. Clark, G. Hill, Photocurrent spectroscopy of InAs/GaAs self-assembled quantum dots, Phys. Rev. B. 62 (2000) 16784–16791. https://doi.org/10.1103/PhysRevB.62.16784.

[27] T. Ivanov, V. Donchev, K. Germanova, P.F. Gomes, F. Iikawa, M.J.S.P. Brasil, M. Cotta, Optical properties of multi-layer type II InP/GaAs quantum dots studied by surface photovoltage spectroscopy, J. Appl. Phys. 110 (2011) 064302. https://doi.org/10.1063/1.3638705.

[28] F. Iikawa, V. Donchev, T. Ivanov, G.O. Dias, L.H.G. Tizei, R. Lang, E. Heredia, P.F. Gomes, M.J.S.P. Brasil, M. a Cotta, D. Ugarte, J.P. Martinez Pastor, M.M. de Lima, a Cantarero, Spatial carrier distribution in InP/GaAs type II quantum dots and quantum posts., Nanotechnology. 22 (2011) 065703. https://doi.org/10.1088/0957-4484/22/6/065703.

[29] M.K.K. Nakaema, F. Iikawa, M.J.S.P. Brasil, E. Ribeiro, G. Medeiros-Ribeiro, W.C. Jr., M.Z. Maialle, M.H. Degani, On the origin of the blueshift from type-II quantum dots emission using microphotoluminescence, Appl. Phys. Lett. 81 (2002) 2743. https://doi.org/10.1063/1.1511812.

[30] M.P.F. de Godoy, M.K.K. Nakaema, F. Iikawa, M.J.S.P. Brasil, J.M.J. Lopes, J.R.R. Bortoleto, M.A. Cotta, R. Magalhães-Paniago, M.J. Mörschbächer, P.F.P. Fichtner, Structural and optical properties of InP quantum dots grown on GaAs(001), J. Appl. Phys. 101 (2007) 073508.

https://doi.org/10.1063/1.2718869.

[31] I. Leontis, M.A. Botzakaki, S.N. Georga, A. G. Nassiopoulou, High capacitance density MIS capacitor using Si nanowires by MACE and ALD alumina dielectric, J. Appl. Phys. 119 (2016) 244508. https://doi.org/10.1063/1.4954883.

[32] S.K. Srivastava, C.M.S. Rauthan, V. Kumar, P.K. Singh, Aperiodic Silicon Nanowire Arrays: Fabrication, Light Trapping Properties and Solar Cell Applications, in: M. Husain, Z. Khan (Eds.), Adv. Nanomater. Adv. Struct. Mater. Vol.79, Springer, New Delhi, 2016: pp. 329–363. https://doi.org/10.1007/978-81-322-2668-0_9.

[33] A.M. Goodman, A Method for the Measurement of Short Minority Carrier Diffusion Lengths in Semiconductors, J. Appl. Phys. 32 (1961) 2550–2552. https://doi.org/10.1063/1.1728351.

[34] R. Kudrawiec, P. Sitarek, M. Gladysiewicz, J. Misiewicz, Y. He, Y. Jin, G. Vardar, A.M. Mintarov, J.L. Merz, R.S. Goldman, K.-M. Yu, W. Walukiewicz, Surface photovoltage and modulation spectroscopy of E− and E+ transitions in GaNAs layers, Thin Solid Films. 567 (2014) 101–104. https://doi.org/10.1016/j.tsf.2014.07.052.

[35] B. Bansal, A. Kadir, A. Bhattacharya, B.M. Arora, R. Bhat, Alloy disorder effects on the room temperature optical properties of GaInNAs quantum wells, Appl. Phys. Lett. 89 (2006) 032110. https://doi.org/10.1063/1.2227618.

[36] M. Galluppi, L. Geelhaak, H. Riechert, Band offsets analysis of dilute nitride single quantum well structures employing surface photo voltage measurements, J. Electron. Mater. 2006 354. 35 (2006) 733–737. https://doi.org/10.1007/S11664-006-0130-0.

[37] M. Galluppi, L. Geelhaar, H. Riechert, M. Hetterich, A. Grau, S. Birner, W. Stolz, Bound-to-bound and bound-to-free transitions in surface photovoltage spectra: Determination of the band offsets for $In_xGa_{1-x}As$ and $In_xGa_{1-x}As_{1-y}N_y$ quantum wells, Phys. Rev. B - Condens. Matter Mater. Phys. 72 (2005) 155324. https://doi.org/10.1103/PhysRevB.72.155324.

[38] N. Shtinkov, P. Desjardins, R. Masut, Empirical tight-binding model for the electronic structure of dilute GaNAs alloys, Phys. Rev. B. 67 (2003) 081202. https://doi.org/10.1103/PhysRevB.67.081202.

[39] V. Donchev, M. Milanova, J. Lemieux, N. Shtinkov, I.G. Ivanov, Surface photovoltage and photoluminescence study of thick

Ga(In)AsN layers grown by liquid-phase epitaxy, J. Phys. Conf. Ser. 700 (2016) 012028. https://doi.org/10.1088/1742-6596/700/1/012028.

[40] J.S. Misiewicz, J., Kudrawiec, R., Gladysiewicz, M., Harris, Electromodulation Spectroscopy of GaInNAsSb/GaAs Quantum Wells: The Conduction Band Offset and the Electron Effective Mass Issues, in: A. Erol (Ed.), Dilute III-V Nitride Semicond. Mater. Syst., Springer, Berlin Heidelberg, 2008: pp. 163–180.

[41] L.F. Bian, D.S. Jiang, P.H. Tan, S.L. Lu, B.Q. Sun, L.H. Li, J.C. Harmand, Photoluminescence characteristics of GaAsSbN/GaAs epilayers lattice-matched to GaAs substrates, Solid State Commun. 132 (2004) 707–711. https://doi.org/10.1016/j.ssc.2004.09.016.

[42] T.S. Wang, J.T. Tsai, K.I. Lin, J.S. Hwang, H.H. Lin, L.C. Chou, Characterization of band gap in GaAsSb/GaAs heterojunction and band alignment in GaAsSb/GaAs multiple quantum wells, Mater. Sci. Eng. B. 147 (2008) 131–135. https://doi.org/10.1016/j.mseb.2007.09.075.

[43] V. Donchev, M. Milanova, I. Asenova, N. Shtinkov, D. Alonso-Álvarez, A. Mellor, Y. Karmakov, S. Georgiev, N. Ekins-Daukes, Effect of Sb in thick InGaAsSbN layers grown by liquid phase epitaxy, J. Cryst. Growth. 483 (2018) 140–146. https://doi.org/10.1016/j.jcrysgro.2017.11.023.

[44] B. V Volovik, N. V Kryzhanovskaya, D.S. Sizov, A.R. Kovsh, A.F. Tsatsul' nikov, J.Y. Chi, J.S. Wang, L. Wei, V.M. Ustinov, Effect of carrier localization on the optical properties of MBE-grown GaAsN/GaAs heterostructures, Semiconductors. 36 (2002) 997–1000. https://doi.org/10.1134/1.1507281.

[45] J.E. Fouquet, A.E. Siegman, Room-temperature photoluminescence times in a GaAs/$Al_xGa_{1-x}As$ molecular beam epitaxy multiple quantum well structure, Appl. Phys. Lett. 46 (1985) 280–282. https://doi.org/10.1063/1.95658.

[46] Y.T. Lin, T.C. Ma, T.Y. Chen, H.H. Lin, Energy gap reduction in dilute nitride GaAsSbN, Appl. Phys. Lett. 93 (2008) 171914. https://doi.org/10.1063/1.3009199.

[47] M. Milanova, V. Donchev, K.L. Kostov, D. Alonso-Álvarez, P. Terziyska, G. Avdeev, E. Valcheva, K. Kirilov, S. Georgiev, Study of GaAsSb:N bulk layers grown by liquid phase epitaxy for solar cells applications, Mater. Res. Express. 6 (2019) 075521.

https://doi.org/10.1088/2053-1591/ab179f.

[48] V. Donchev, M. Milanova, Dilute nitrides heterostructures grown by liquid phase epitaxy for solar cells applications, J. Phys. Conf. Ser. 1762 (2021) 012025. https://doi.org/10.1088/1742-6596/1762/1/012025.

[49] J. Li, S. Iyer, S. Bharatan, L. Wu, K. Nunna, W. Collis, K.K. Bajaj, K. Matney, Annealing effects on the temperature dependence of photoluminescence characteristics of GaAsSbN single-quantum wells, J. Appl. Phys. 98 (2005) 013703. https://doi.org/10.1063/1.1931032.

[50] K. Nunna, S. Iyer, L. Wu, J. Li, S. Bharatan, X. Wei, R.T. Senger, K.K. Bajaj, Nitrogen incorporation and optical studies of GaAsSbN/GaAs single quantum well heterostructures, J. Appl. Phys. 102 (2007) 053106. https://doi.org/10.1063/1.2777448.

[51] T.W. Kim, Y. Kim, K. Kim, J.J. Lee, T. Kuech, L.J. Mawst, 1.25-eV GaAsSbN/Ge double-junction solar cell grown by metalorganic vapor phase epitaxy for high efficiency multijunction solar cell application, IEEE J. Photovoltaics. 4 (2014) 981–985. https://doi.org/10.1109/JPHOTOV.2014.2308728.

[52] A. Gonzalo, L. Stanojević, A.D. Utrilla, D.F. Reyes, V. Braza, D. Fuertes Marrón, T. Ben, D. González, A. Hierro, A. Guzman, J.M. Ulloa, Open circuit voltage recovery in GaAsSbN-based solar cells: Role of deep N-related radiative states, Sol. Energy Mater. Sol. Cells. 200 (2019) 109949. https://doi.org/10.1016/j.solmat.2019.109949.